LT-XFD_CDR_XPD-00122

NSLS-II Project

CONCEPTUAL DESIGN REPORT for the

HARD X-RAY NANOPROBE BEAMLINE AT NSLS-II

final draft Sep 2009

Intentionally blank.

Approvals and Reviewers

Compiled by	**Signature**	**Date**
Yong S. Chu, Beamline Scientist, NSLS-II		
Approved		
Qun Shen, XFD Director, NSLS-II		
Reviewers		
Cev Ismail Noyan, BAT Spokesperson, on behalf of the BAT		
Andy Broadbent, Beamlines Manager		
Nicholas Gmür, ESH Coordinator, NSLS-II		
Sushil Sharma, Mechanical Engineering Group Leader, NSLS-II		

Document Updates

The Conceptual Design Report for the Hard X-ray Nanoprobe (HXN) Beamline at NSLS-II is a controlled document, revised under change control.

Version No.	Date	Changes made
1	10-1-2009	final draft, submitted to BAT

Intentionally blank.

Contents

1 INTRODUCTION 7

1.1 SCIENTIFIC REQUIREMENTS 7

1.2 THE HXN TEAM 9

1.3 BEAMLINE ADVISORY TEAM (BAT) 10

2 BEAMLINE LAYOUT 11

2.1 OVERVIEW 11

2.2 INSERTION DEVICE 12

2.3 FRONT END 16

2.4 OPTICAL LAYOUT 17

2.5 HIGH HEATLOAD OPTICS 29

2.6 LIST OF MAJOR COMPONENTS 31

2.7 SUMMARY OF BEAMLINE PERFORMANCE SPECIFICATIONS 32

3 ENDSTATION INSTRUMENTATION 34

3.1 KEY REQUIREMENTS OF THE HXN MICROSCOPE 34

3.2 HXN DETECTORS 35

4 SPECIAL BEAMLINE REQUIREMENTS 36

4.1 SATELLITE BUILDING AND ENDSTATION 36

4.2 DATA TRANSFER RATES 37

5 FUTURE UPGRADE OPTIONS ..... **ERROR! BOOKMARK NOT DEFINED.**

APPENDIX 1: SCHEDULE 38

CONSTRUCTION OF HXN BEAMLINE 38

PLANNED TASKS AND MILESTONES FOR 1NM SPATIAL RESOLUTION R&D 38

PLANNED TASKS AND MILESTONES FOR NANOPOSITIONING R&D 39

APPENDIX 2: CONSIDERATIONS FOR HXN BEAMLINE SITE 40

M.1: NSLS-II SITE SPATIAL VARIABILITY OF GROUND VIBRATION 41

M.2 FIELD TEST FOR "EXTREME" TRAFFIC ON BROOKHAVEN AVE. AND INFLUENCE ON NANOPROBE 43

APPENDIX 3 LIST OF BEAMLINE COMPONENTS 48

APPENDIX 4 REFERENCE DRAWINGS 50

Acronyms

APS	Advanced Photon Source
DCM	Double Crystal Monochromator
FE	Front End
FEA	Finite Element Analysis
FOE	First Optics Enclosure
HXN	Hard X-ray Nanoprobe beamline
IVU	In-Vacuum Undulator
LOB	Lab-Office Building
LOI	Letter of Intent
MLL	Multi Layer Laue lens
RSI	Requirements, Specifications, and Interfaces

1 INTRODUCTION

1.1 Scientific Requirements

The hard x-ray nanoprobe beamline and endstation instruments (HXN) will be designed and constructed to explore new frontiers of hard x-ray microscopy applications with the highest achievable spatial resolution. Currently the available spatial resolution for scientific applications, provided by scanning x-ray microscopes in the hard x-ray regime, is limited to ~30nm, which is still insufficient for probing the nanoscale interfacial structures critical in determining properties and functionalities of material and biological systems. The HXN beamline aims to enable x-ray experiments at spatial resolutions ranging from 30 nm to its ultimate goal of ~1 nm. The proposed range of the spatial resolution will effectively bridge the current gap between x-ray microscopy and electron microscopy, opening up new scientific opportunities. The ability to adjust the spatial resolution between 1 nm and 100 nm is crucial in studying how structural hierarchy is related to the functional properties of materials. This relationship between hierarchical structure and properties is known to exist in nearly all classes of materials, from metals to biological samples, and is a key component in furthering the development of the next generation of technological materials. In order to achieve this unprecedented spatial resolution and sensitivity, the HXN beamline and endstation instruments will be designed as a scanning microscope, taking full advantage of the high brightness offered by the NSLS-II lattice.

The letter of intent (LOI) for the HXN beamline elaborated four key modalities of x-ray microscopy, which have been fully endorsed by the HXN beamline advisory team as well as the EFAC and DOE review panels. These are:

- x-ray fluorescence
- nanodiffraction
- coherent diffraction imaging
- differential phase-contrast imaging

Photon-stimulated x-ray fluorescence offers one of the most sensitive ways to detect the presence of specific atomic elements embedded within a hosting matrix. The proposed x-ray energy range of the HXN beamline, 6-25 keV, enables detection of most of the elements in the periodic table through the fluorescence process induced by K or L-edge excitation. The ability to detect extremely low quantities of isolated atoms or small clusters of atoms is extremely important in understanding how small concentration of impurities in semiconducting or condensed materials affects electronic, magnetic, or catalytic properties of the hosting matrix. In addition, the ability to image and quantify trace metal distribution in cells and tissues is extremely important in understanding metal-mediated biological processes, including understanding many diseases and the development of therapeutic and diagnostic agents to treat them. The ultimate goal is to explore the x-ray fluorescence detection with single atom sensitivity.

Diffraction is an essential structural tool to quantify crystalline phase, strain, orientation, and texture. At the atomic level, virtually all hard materials organize themselves in crystalline form at varying length scales when thermally annealed, and the spatial arrangement of the crystalline grains and grain boundaries can profoundly influence the material properties. Unlike the x-ray fluorescence process, the diffraction process channels the incident x-rays into well-defined directions, thereby providing high measurement efficiency without collecting signals over a large solid angle. Virtually all nanodiffraction investigation requires simultaneous measurement of the x-ray fluorescence signal in order to validate the positioning accuracy of the probe and quantifying the structural environment around the crystalline phase. Consequently, x-ray fluorescence and nanodiffraction are complementary tools, extremely valuable for nanoscale structural characterization of hard materials.

Coherent diffraction imaging is a powerful and fast-growing technique, with its ultimate spatial resolution limited only by the wavelength of the x-ray. There are several varieties of this imaging modality, classified by the type of sample (crystalline vs. noncrystalline) and the details on how the reconstruction is carried out. All types of coherent diffraction imaging have demonstrated extreme sensitivity for weakly absorbing specimens with a demonstrated spatial resolution below 10nm. With this potential to reach nanometer spatial resolution in the low contrast materials, coherent diffraction imaging is an important complementary technique at the HXN beamline. In

particular, it is feasible to combine x-ray fluorescence measurement with coherent diffraction imaging in a ptychography method in order to produce both spectroscopic and electronic density images from a single experiment. In addition, the far-field data collected in this way can be used for differential phase-contrast imaging by performing straightforward manipulation of the digital data set without reconstruction, to provide high-throughput direct imaging.

An important aspect of these different x-ray microscopy techniques is that they are mutually compatible with one another, providing feasibility for implementing methods to perform simultaneous or parallel measurements with two or more different techniques. This is an important instrumentation approach, because the intense photon density over the focal spot can lead to significant radiation damage for soft and even some of the hard materials. Acquiring as much information from the specimen over a given exposure time will be one of the key instrumentation principles in developing a HXN microscope.

One important scientific question regarding the ultimate performance of the HXN beamline is the feasibility for detecting single-atom fluorescence. Obviously, the answer to this question depends on the performance level of different components of this complex instrument, including the source brightness, beamline optics (i.e., mirrors and monochromator), focal spot size and focusing efficiency, structural details in the sample, stability of the beamline and microscope, solid angle and detection efficiency of the fluorescence detector. However, it would be interesting to carry out a rather crude order-of-magnitude estimate, in order to estimate the ultimate feasibility. The expected brightness of NSLS-II's U20 undulator at 10keV is $8x10^{20}$ ph/s/0.1%bw/mm^2/mrad^2, with horizontal and vertical emittance values of 0.5 nm-rad and 0.008nm-rad, respectively. This gives a total coherent flux of $3.1x10^{12}$ ph/s/0.1%bw at 10 keV. If one assumes the following conditions, the expected flux density is $2x10^{10}$/nm^2.

- Beamline has 50% transmission efficiency (including mirror and monochromator reflectivity and window transmission)
- Beamline optics can deliver 50% of the available coherent flux onto the nanofocusing MLL (multilayer Laue lens) optics
- MLL optics can produce a 1nm focused beam with 20% efficiency
- MLL optics have the number of layers matched to the energy band pass of a Si(111) monochromator

The combined x-ray fluorescence cross-section of a single Zn atom excited by 10keV x-rays is $1.0x10^4$ barns or $1.0x10^{-6}$ nm^2. Thus, the total emitted fluorescence count rate is $2.0x10^4$ ph/s. If an energy dispersive detector can integrate 20% of 4π SR with 100% efficiency, the measured count rate would be 4,000 counts/sec. It is import to point out that the background signal due to scattering is not considered in this estimate. Of course, the greatest uncertainties in bringing the abovementioned scenario into practice reside in the ultimate performance of the nanofocusing optics. However, this estimate provides the target performance levels for different optical components at the HXN beamline that will guide the design and construction of the beamline.

Designing, building, and operating the HXN beamline are intimately connected to the two critical instrumental challenges: development of high spatial resolution nanofocusing optics, and development of an x-ray microscope with adequate positioning and scanning capabilities. In order to tackle the technical challenges, NSLS-II has launched two major R&D programs: development of 1nm spatial resolution x-ray optics and development of a nanopositioning capability adequate for 1nm x-ray microscopy. These R&D programs are making steady progress with high hopes of fulfilling the targeted goals. Recently, HXN team members, along with the collaborators at the APS and CNM, achieved the first 2D focused x-ray beam with a sub-100nm size in FWHM, which is an encouraging first experimental verification that MLL optics can be used for a 2D focused beam. The x-ray nanofocusing research is evolving rapidly and several groups in the world are developing novel technologies with the goal to achieve nm-scale focus. This includes the latest results from Japan based on multilayer mirrors, where a 15nm line focus has been demonstrated. In order to ensure the capability to accommodate these developments in the future, the conceptual design of the HXN beamline has been considerably modified in order to provide sufficient flexibility, so that the beamline does not have any potential technical limitations for taking full advantage of other types of nanofocusing optics, if a significant technical breakthrough should occur in the near future.

What separates the HXN beamline from the other existing x-ray microscopy facilities is the detailed attention paid to the vibration environment around the HXM microscope and the HXN endstation. Even at earlier planning stages, significant technical considerations were given to providing the best environment for the HXN endstation instruments. Extensive vibration measurements and numerical simulations have been performed to guide the planning of the HXN beamline site, the location and structural configuration of the satellite building, and the endstation housed within. Recently, a similar level of attention has been given to the temperature stability around the microscope and possible methods to suppress or damp out the acoustic and vibration noise from the users of the HXN beamline. The conceptual design of the HXN beamline is optimized with the physical boundary conditions required to construct a satellite building physically isolated from the potential noise sources from the NSLS-II storage ring, experimental hall, and the adjacent lab-office building.

In summary, the HXN beamline aims to become a world-leading scanning microscopy facility, enabling the highest spatially resolved structural and spectroscopic x-ray imaging techniques on day 1 with unprecedented elemental sensitivity, with the ultimate goal of achieving ~1nm spatial resolution. The x-ray microscopy techniques provided at the HXN beamline will open new frontiers of hard x-ray microscopy applications in interdisciplinary scientific fields ranging from materials science, environment science, biology, nano-catalysis, and x-ray physics. The conceptual design aims to meet extremely demanding scientific and technical requirements for achieving the highest level of detection sensitivity, delivering the highest level of available coherent flux onto the nanofocusing optics by carefully considering and optimizing the stability against the potential mechanical and thermal induced drifts.

1.2 The HXN Team

The Hard X-ray Nanoprobe beamline at NSLS-II plans to achieve scientific and technical goals that are beyond the current state-of-the-art. As mentioned earlier, development and construction of the HXN beamline is coordinated with two supporting R&D projects: 1nm Spatial Resolution R&D and Nanopositioning R&D. Consequently, the HXN Team consists of many members. It is also important to acknowledge that the effort for developing high spatial resolution multilayer Laue lenses (MLLs) initially started at the Advanced Photon Source (APS) and the Center for Nanomaterials (CNM) at Argonne National Laboratory. The HXN team members are actively engaged in continuing collaboration. The following list summarizes the HXN team and multi-faceted support and collaboration.

HXN Beamline

Yong Chu: Group leader
Lawrence Margulies: Beamline scientist
Ken Evans-Lutterodt: MOU staff from NSLS and Kinoform development
Steve O'Hara: Beamline mechanical engineer

1nm Spatial Resolution R&D

Ray Conley: MLL fabrication, processing and metrology
Hanfei Yan: MLL theory and testing
Enju Lima: MLL testing using coherent phase retrieval methods
Nathalie Bouet (postdoc): MLL processing
James Biancarosa (technician): MLL fabrication

Nanopositioning R&D

Evgueni Nazaretski: Nanopositioning development

Other Support

Andy Broadbent: Interfacial management and coordination
Nikolaos Simos: Vibration measurement, analysis and modeling
Brian Mullany: Technical drawing and designing support
Oleg Chubar: Numerical Simulations on Undulator Radiation
Viswanath Ravindranath: Numerical Simulations on High Heatload Optics

External Collaboration

Jörg Maser: APS/CNM collaboration on MLL theory and experiment
Albert Macrander: APS collaboration on MLL fabrication and metrology
Deming Shu: APS collaboration on Nanopositioning
Volker Rose: APS collaboration on x-ray characterization of MLLs
Chian Liu: APS collaboration on MLL fabrication
Nima Jihedi: APS collaboration on metrology

1.3 Beamline Advisory Team (BAT)

The beamline advisory team of the Hard X-ray Nanoprobe beamline commands significant expertise in x-ray microscopy, synchrotron instrumentation, and a wide array of x-ray microscopy applications in interdisciplinary scientific fields. The HXN BAT members not only advise on the development of the HXN beamline and its endstation instruments but also play a crucial role in representing scientific interests in different fields, including materials science, nanoscience, environmental science, and biological science. The current HXN BAT members are listed below.

Table 1.3: HXN Beamline Advisory Team

Cev Ismail Noyan (spokesperson)	Columbia University
Chris Jacobsen	Stony Brook University
Don Bilderback	Cornell University
Tonio Buonassisi	Massachusetts Institute of Technology
Ken Evans-Lutterodt	Brookhaven National Laboratory
Peter Sutter	Brookhaven National Laboratory
Tony Lanzirotti	University of Chicago
Stefan Vogt	Argonne National Laboratory
Martin Holt	Argonne National Laboratory

2 BEAMLINE LAYOUT

2.1 Overview

The conceptual design of the HXN beamline is based on a few important underlying considerations. As mentioned in the previous section, the conceptual design of the HXN beamline ensures sufficient flexibility in its optical layout to accommodate different types of nanofocusing optics. For example, multilayer Laue lenses have the potential of the reaching the highest spatial resolution with a compact design. However, the lateral dimension of the MLL is likely to be no larger than ~100 μm, due to the extreme technical challenge associated with fabricating a large optic keeping the zone placement sufficiently smaller than its outmost zone width. A Fresnel zone plate is an extremely convenient optic, adopted in many x-ray microscopes. But it requires that the source-to-optic distances in the horizontal and vertical directions are sufficiently close to each other, in order to avoid astigmatism. Astigmatism is not a problem for MLLs and nanofocusing KB mirrors, for the focal length for each direction can be chosen separately. On the other hand, nanofocusing KB mirrors tend to require a longer working distance because of the length of the two mirrors. The optical constraint of kinoforms is similar to MLLs or KBs, depending on whether they are fabricated in a short or long form. By creating a secondary source at two possible locations from the primary source, the conceptual design of the HXN beamline offers different modes of operation. These modes provide different ranges of the transverse coherence length at the plane of the nanofocusing optic, making it possible to optimize the utilization of the available coherent flux for different types of focusing optics. Section 2.4 will be devoted to elaborating how these modes can be implemented.

The second important design consideration of the HXN beamline is for overall beamline stability against possible source motion and thermal drift. The HXN beamline employs a secondary source aperture to create a secondary x-ray source with a well-defined source size in both the horizontal and vertical directions. A mechanically stable secondary source aperture will greatly reduce or even eliminate possible source motion—whether actual, or induced by the vibration or thermal drift of the high-heat load optics, located upstream. The ability to change the size of the secondary source offers an easy way to control the transverse coherence length at the plane of the nanofocusing optics, providing a straightforward way to trade the focused flux for the focus size. For example, a small secondary source size, producing a transverse coherence length larger than the lateral dimension of the focusing optic, meets a sufficient condition for a diffraction-limited spot size. On the other hand, a larger secondary source size, under the identical focusing conditions, will result in more focused flux with a larger spot size.

The third consideration is on the environment of the nanofocusing experiments. The HXN endstation will be constructed in order to provide effective means to reduce and manage the ambient vibration, acoustic noise, and temperature drift, so that the diffraction-limited beam size can be maintained over sufficiently long times (> 12 hrs). Intensive investigations have been carried out by making actual measurements of the ground vibrations at various locations around the NSLS-II site and by numerically simulating the effects of vibrations from the major sources within and around the storage ring structure and the laboratory-office-building (LOB). These results provide sufficient scientific justification that the best way to isolate or reduce the ambient vibrations is to house the HXN microscope within a satellite building, physically separated from the storage ring and nearby LOB. The conceptual design utilizes a distance of 108m from the synchrotron source to the nanofocusing optic, in order to allow a separate satellite building structure to house the HXN microscope while optimizing the utilization of the available coherent flux for nanofocusing.

The structural overview of the HXN beamline is shown in Figure 2.1.1. It will use a low beta storage ring straight section with an in-vacuum undulator with a 20 mm period (IVU20). Its FOE spans from the end of the ratchet wall at z=25.5m to z=40.0m, containing beam conditioning optical components and beam diagnostic components. The monochromatic hutch is located in the experimental hall, occupying from z=57.5m to z=64.5m. The monochromatic hutch will be primarily used for beamline diagnostics and developing beam position monitoring methods to stabilize the x-ray beam, in order to keep the focus fixed onto a constant point on a sample. The endstation will be a monochromatic hutch, spanning from z=93m to z=113m, with interior dimensions 20m long, 5m wide, and 3.5m high. The HXN microscope will be located in the endstation. A blue boundary shown in Figure 2.1.1 represents a tentative floor structure of the HXN satellite building. A specification summary on the satellite

building is found in section 4. More complete specifications on the satellite building can be found in Experimental Facilities Requirements, Specifications and Interfaces (RSI) document for the Hard X-ray Nanoprobe Beamline Satellite building. This document will be available as a reference document. Detailed descriptions of the optical layout and components are found in section 2.4.

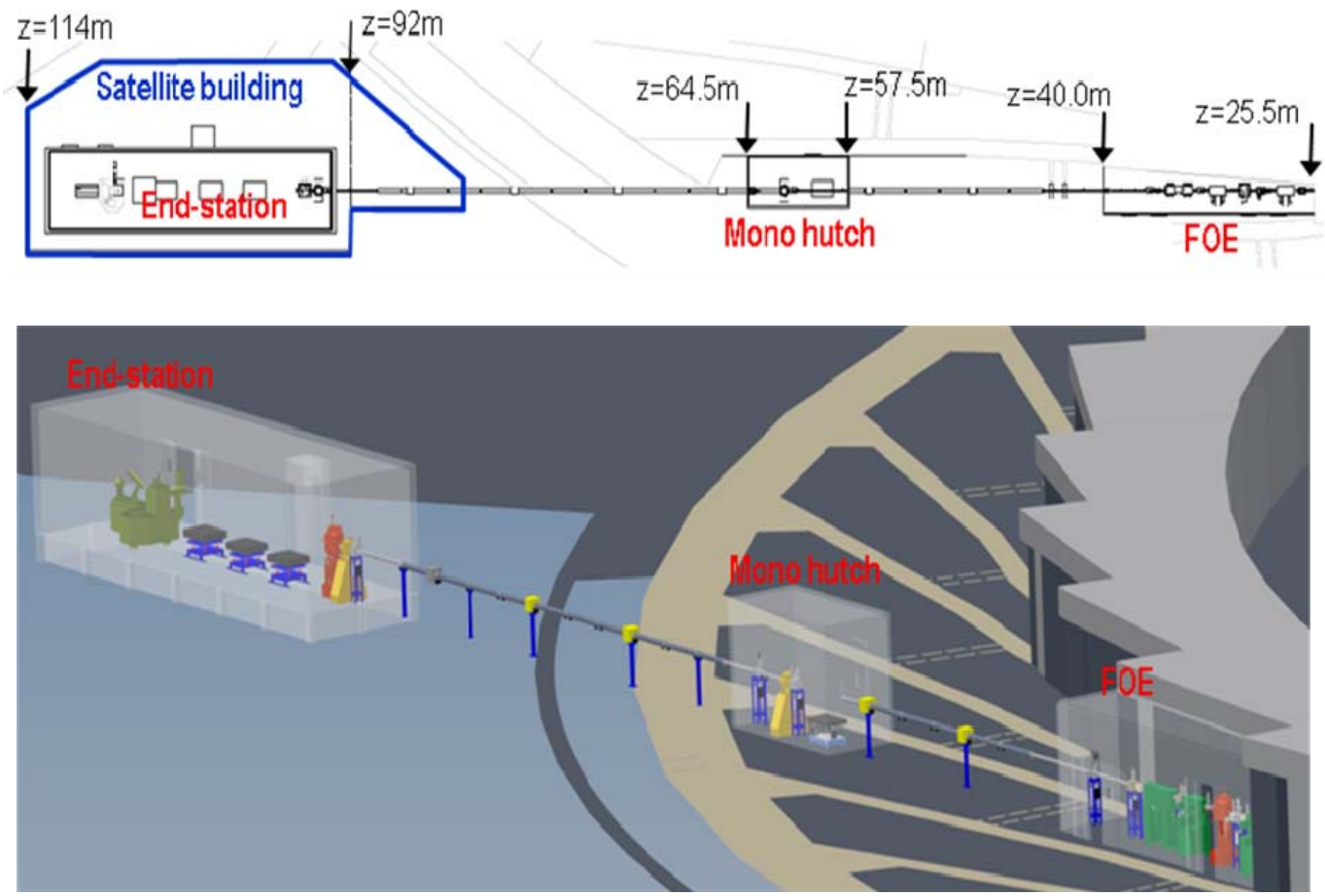

Figure 2.1.1. Structural overview of the Hard X-ray Nanoprobe beamline. The planar (top) and 3D (bottom) drawings show the position and overall size of the first optical enclosure (FOE), the monochromatic hutch, and the endstation. The endstation is located within a satellite building, physically separated from the storage ring building and a nearby lab-office-building (LOB), in order to reduce the ambient vibration. A blue boundary indicates the tentative footrprint of the satellite building.

2.2 Insertion Device

The scientific goal of the HXN beamline demands the highest achievable source brightness over its operating energy range from 6 to 25 keV. The brightness, defined as the flux output per unit bandwidth (0.1%), per unit source area, and per unit solid angular divergence, is the single most important source parameter for x-ray microscopy. The total amount of flux over the diffraction-limited focused spot is limited to the total amount of the coherent flux from a synchrotron source. The coherent flux, F_c, is related to the on-axis source brightness, B, by the following relationship, $F_c = B(\lambda/2)^2$, where λ is the x-ray wavelength. Consequently, higher source brightness gives higher coherent flux and, consequently, higher integrated flux over a diffraction-limited focused beam spot.

Among the available insertion devices as shown in Figure 2.2.1, the in-vacuum undulator (IVU20) located at the low beta section, is the most logical choice for the HXN beamline, based on the brightness comparison. The basic parameters for an IVU20 device are listed below.

- emittance: ε_H = 0.5 nm, ε_V = 0.008 nm
- beta function: $\beta_H \approx 2$ m, $\beta_V \approx 1$ m
- electron source parameters:
- σ_h=31.8μm, $\sigma_{h'}$=15.7μrad
- σ_v =2.9 μm, $\sigma_{v'}$ = 2.8 μrad
- period length: 20 mm
- number of periods: 148
- device length: 3.0m
- minimum magnetic gap: 5 mm
- peak magnetic field strength, B: 1.03T
- maximum K: 1.83
- maximum total power: 9.1 kW
- on-axis power density: 65.4 kW/mrad^2

During the initial operation phase, ε_H = 0.9 nm, ε_V = 0.008 nm will be used. A larger value of the horizontal emittance will results in σ_h=42.6μm and σ_h=21.1μm with no impact in the vertical direction.

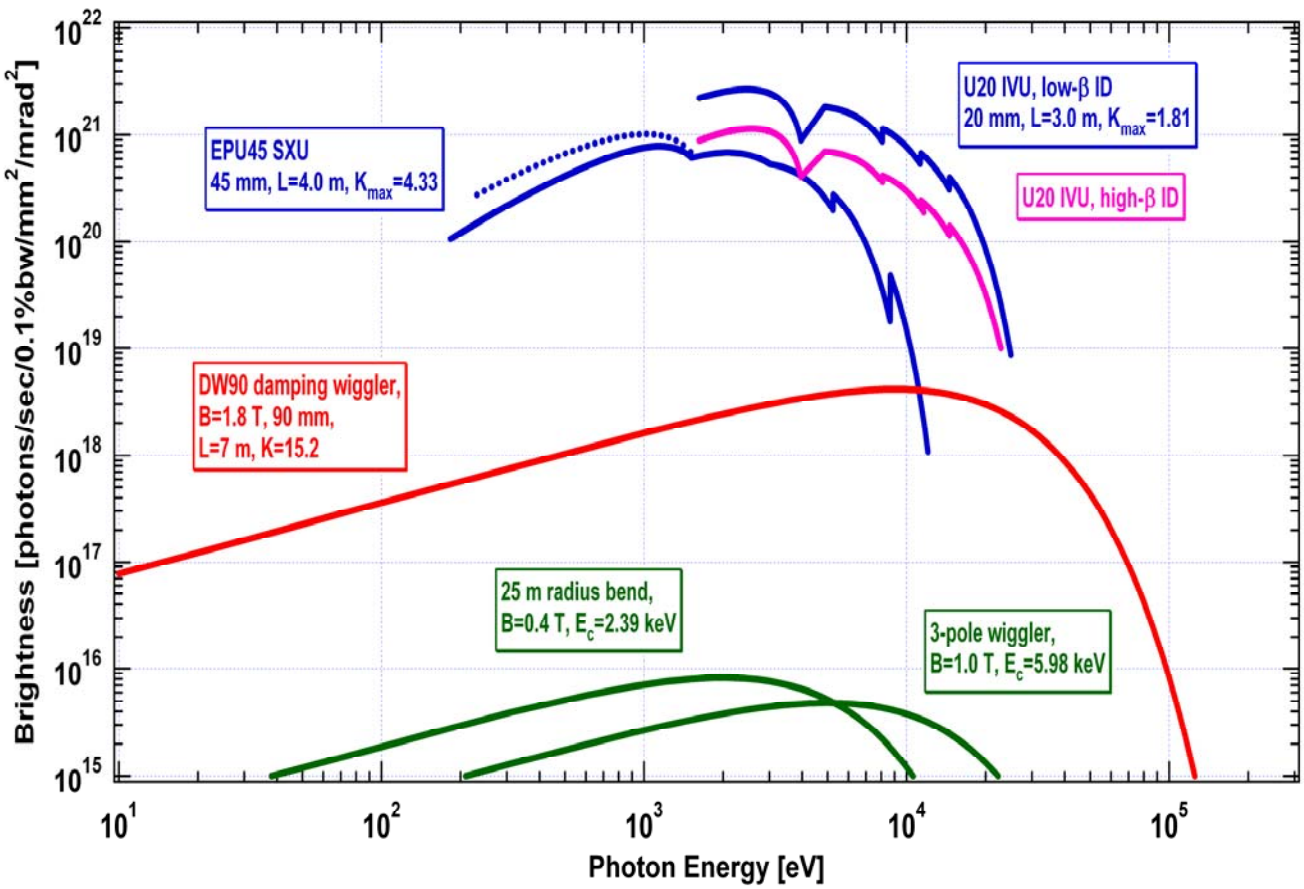

Figure 2.2.1: Brightness vs. Photon energy for the baseline radiation sources at NSLS-II. Ring parameters: 3.0 GeV, 0.5 A, ε_h=0.5 nm, ε_v=0.008 nm, energy spread=0.001; Straight section parameters: low-β: β_h=2.02 m, β_v=1.06 m; high-β: β_h=20.8 m, β_v=2.94 m; $\alpha_h=\alpha_v=\eta_h=\eta_v=\eta'_h=\eta'_v=0$. This figure was extracted from Chapter 8 of the NSLS-II Conceptual Design Report.

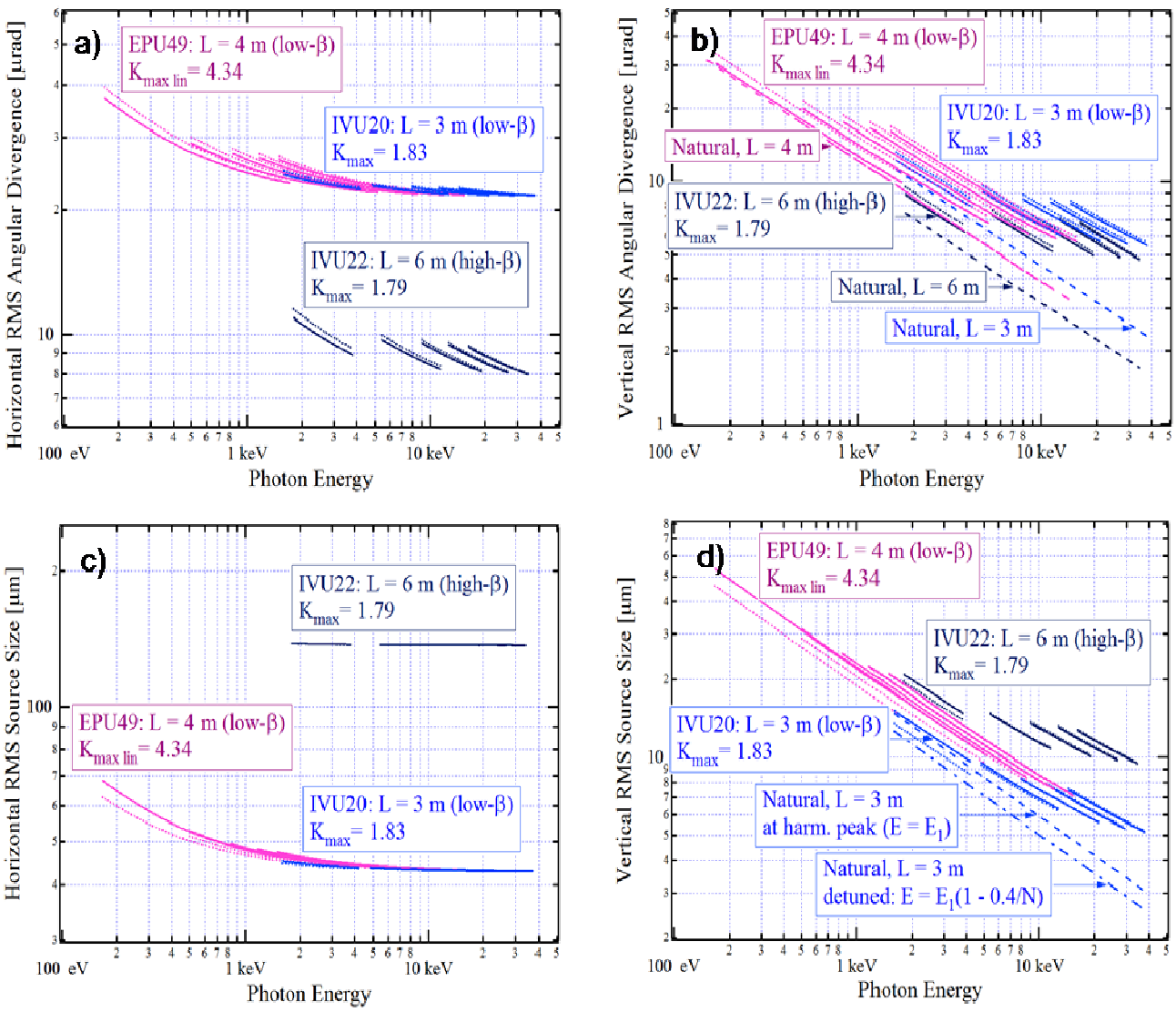

Figure 2.2.2. The RMS x-ray angular and source size of the NSLS-II undulators. a) horizontal angular divergence, b) vertical angular divergence, c) horizontal source size and d) vertical source size. The straight dashed lines represent the effective angular divergences (c) and source size (d) of the single-electron emission.

The estimated source brightness with ε_H = 0.5 nm is 8×10^{20} ph/s/0.1%bw/mm^2/mrad^2 at 10keV and 0.9×10^{20} ph/s/0.1%bw/mm^2/mrad^2 at 20keV, resulting in the total coherent flux of 3.1×10^{12} and 8.7×10^{10} ph/s/0.1%bw at the respective energies. Figure 2.2.2 shows the RMS angular and source size of a few NSLS-II undulator devices with ε_H = 0.9nm . This calculation takes into account of broadening due to finite energy spread and emittance of electron beam. At 10 keV, the estimated FWMS source size and angle are

$$S_h = 101\mu m,\ S_v = 12\ \mu m,\ \theta_H = 53\mu rad,\ \theta_V = 21\mu rad,$$

where S_h, S_v, θ_H, θ_V are the horizontal x-ray source size in FWHM, the vertical x-ray source size in FWHM, the horizontal x-ray source size in FWHM, and the vertical x-ray source angle in FWHM. In the vertical direction, the source angle and size become somewhat larger if the photon energy slightly smaller than the resonance energy of the undulator is chosen in order to increase the flux. With the horizontal emittance of 0.5 nm, the horizontal x-ray source size at 10keV reduces from 101μm to 75 μm and the horizontal x-ray source angle from 53μrad to 40μrad, with no impact in the vertical direction. The above source angle and size are used for the conceptual design as a baseline. The reduction of the horizontal source size and angle resulting from reduction of the horizontal emittance

does not have any impact on the conceptual design, other than the fact that the practical range of the horizontal source aperture will be decreased.

One of the most fundamental considerations for the conceptual design is how to handle the power delivered by the x-rays onto the beamline components, in particular to the x-ray windows, mirrors, and monochromators that are exposed to the white beam from the undulator. A brief summary on the estimated power from IVU20 is given here, so that the high heatload considerations implemented in the conceptual design can be understood easily. Figure 2.3.3 shows the total output power of the NSLS-II as a function of K and the fundamental photon energy.

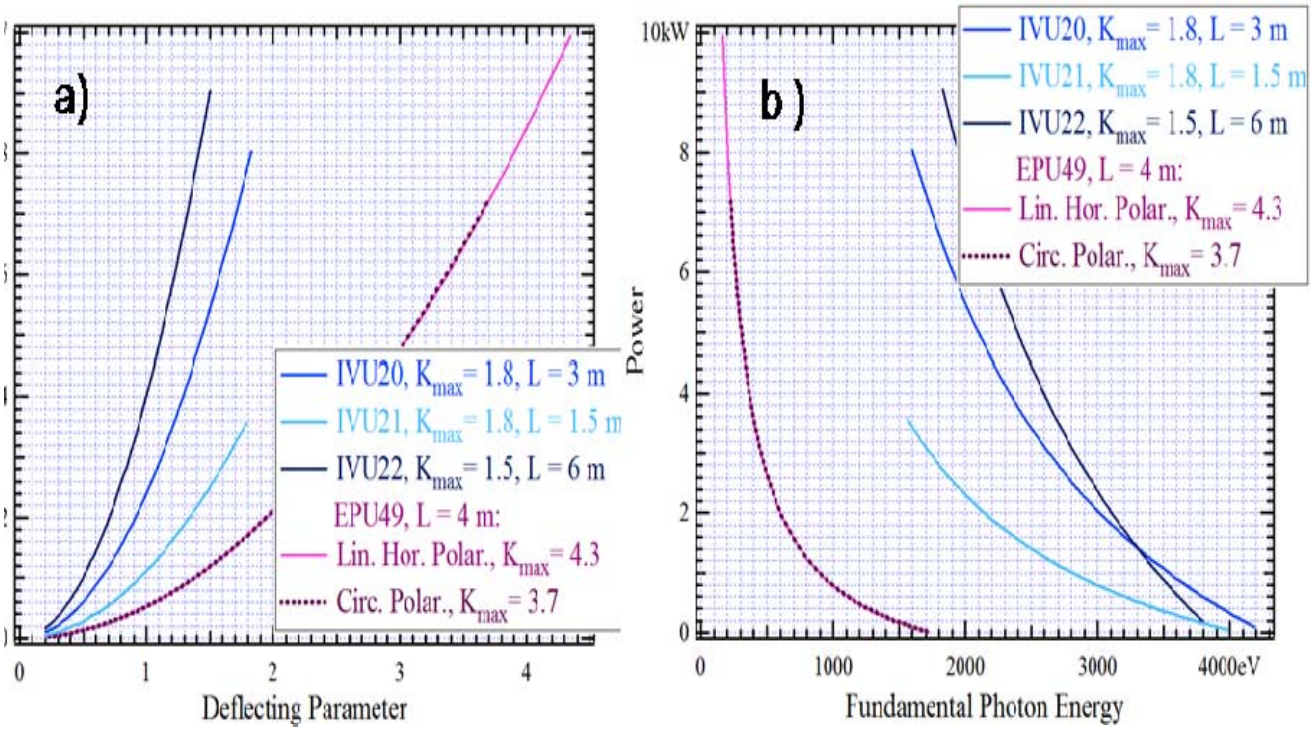

Figure 2.2.3: Total output power of the NSLS-II undulators as functions of a) the undulator deflecting parameter, K, and b) the fundamental photon energy.

For IVU20, the highest power, ~8kW, is produced at the maximum K value of 1.83, corresponding to the minimum gap of 5 mm and the fundamental photon energy of 1.6 keV. Consequently, the same high power condition is also met at higher harmonic x-ray energies, 8 (5th), 11,2 (7th), 14,4 (9th), 17.6 (11th) keV and so on. The total power output depends rapidly on the photon energy. At the fundamental photon energy of 2 keV, the total power is reduced by about 30%.

Fig 2.2.4a (next page) shows the two dimensional angular distribution of the power emitted from an IVU20 at K=1.83. The horizontal (Figure 2.2.4b) and vertical cut (Fig. 2.2.4c) through the center shows that the FWHM widths of the power distribution are ~500 μrad in the horizontal direction and ~200 μrad in the vertical direction.

These are significantly larger than the angular sizes of the central cone. Consequently, the integrated useful monochromatic flux tails off with increasing angular aperture size, while the integrated power increases almost linearly, as shown in Figure 2.2.4d and 2.2.4e. For example, with a fixed vertical angular aperture of 53μrad, corresponding to about a two FWHM angular source size, a horizontal angular aperture of 80μrad integrates more than 80% of available monochromatic flux, accepting 280W of power. On the other hand, by adjusting the horizontal and vertical angular aperture together, it is possible to optimize the acceptance of the useful flux against the accepted power. The conceptual design plans to accept 180W onto the collimating mirror with an angular aperture of 80 μrad (H) x 40 μrad (V). The HXN power management strategy is summarized in section 2.5.

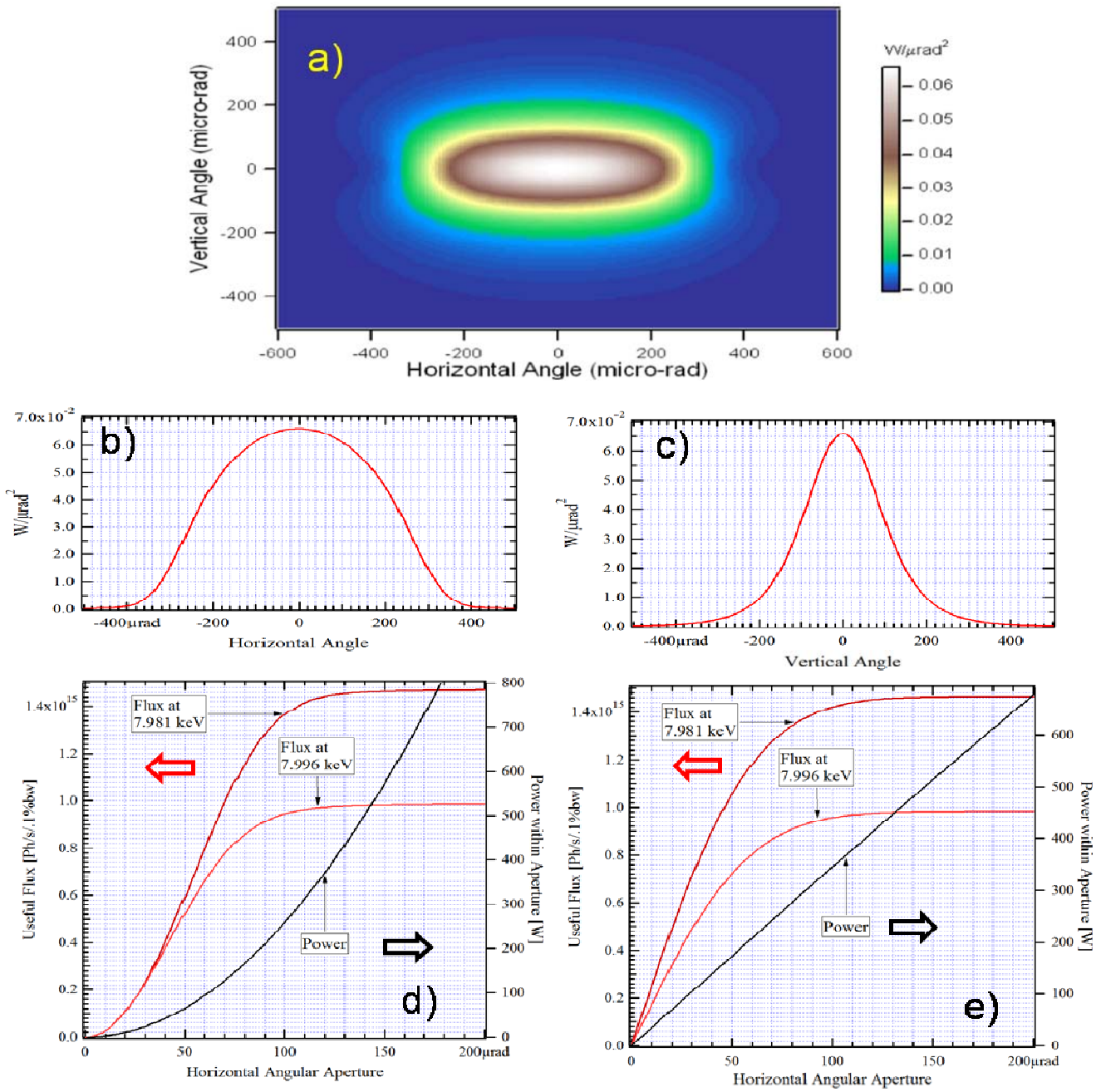

Figure 2.2.4. Angular power distribution emitted by IVU20 at K=1.83. a) 2D angular distribution, b) horizontal cut through the central axis, c) vertical cut through the central axis, d) integrate power and monochromatic flux as a function of the horizontal angular aperture with a fixed vertical angular aperture of 53 μrad, and e) integrate power and monochromatic flux while varying both aperture sizes with a fixed ratio of 1 (horizontal) to 0.4 (vertical) ratio.

2.3 Front End

A standard NSLS-II front end (FE) is shown in Figure 2.3.1. The fixed mask is designed to accept 0.5 mrad in the horizontal direction and 0.3 mrad in the vertical direction. The HXN beamline plans to use the FE XY-slits as its white beam slit. The nominal slit opening will be 50 μrad in the vertical direction and 100 μrad in the horizontal direction. A pair of typical L-shaped white beam slits results in an oval shaped beam instead of a rectangular shape. A sharper corner is needed to create a well-defined rectangular shaped illumination, useful for performing straightforward diagnostic checks for aligning the beamline optics. The standard FE will be described in a separate FE CDR document.

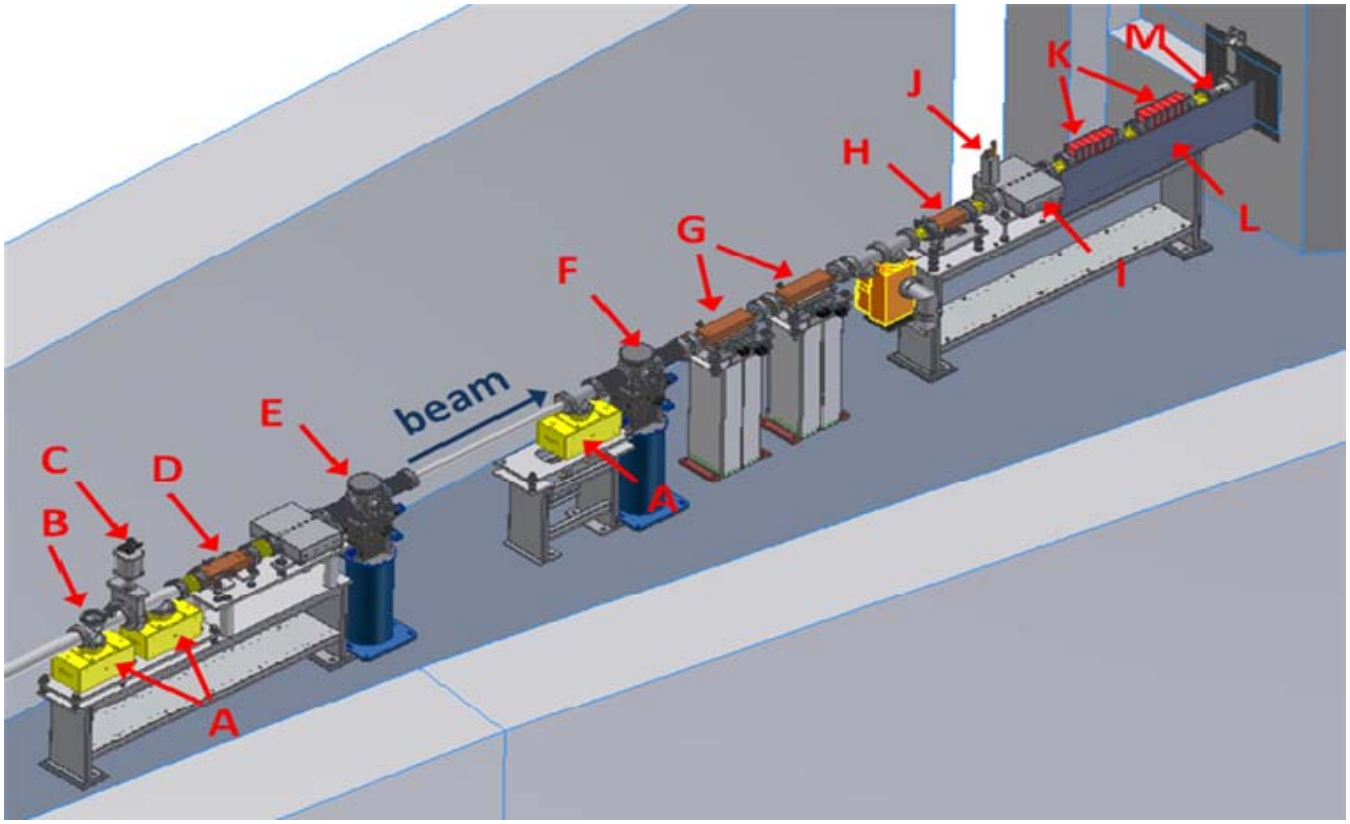

Figure 2.3.1. Configuration of a standard front end. The HXN Beamline will use a standard NSLS-II front end with one modification. The XY slits must be modified so that they have sharp corners, in order to give a square shaped beam. A: ion pump, B: bending magnet photon shutter, C: slow gate value, D: fixed aperture mask, E: X-ray beam position monitor 1, F: X-ray beam position monitor 2, G: XY slits, H: photon shutter, I: safety shutter collimator, J: fast gate value, K: dual safety shutters, L: lead shield, and M: ratchet wall collimator.

2.4 Optical Layout

This is the main section of the conceptual design report, describing the details of the optical components and the rationales for the adopted optical arrangement. Since the optical layout for the hard x-ray nanoprobe beamline is rather sophisticated, this section is subdivided into two parts, in order to provide a more effective illustration. Subsection, "Overview on Major Optical Components" will be devoted to the description of the major optical components and overall justification on why the optical components are arranged in particular ways. Subsection, "Beamline Operation Modes", will elaborate on the optical performance of three possible operations modes, along with simple model calculations.

2.4.1 Overview of Major Optical Components

The schematic overview of the major optical components is shown in Figure 2.4.1. A complete list of the beamline components is found in section 2.7. As explained in section 2.2, the HXN beamline will use an IVU20 undulator in a low-beta section. The HXN beamline will use the XY-slits in the front end (FE) as its white beam slits, in order to limit the power onto the water-cooled horizontal collimating mirror, M1, located at z=27.5m. M1 has a bending capability to collimate the incident x-rays to the horizontal monochromator, in order to reduce the energy dispersion due to the horizontal divergence from the source. M1 also serves as a low band pass filter by rejecting high order harmonics, operating at a fixed incidence angle of 2.70 mrad. With a length of 1m, M1 has a maximum angular aperture of 98 μrad in the horizontal direction. M1 has three different reflecting surfaces, Si, Rh, and Pt, corresponding to cut-off energies of ~11.3, ~22.9 and ~29.4 keV, respectively. Pink beam slits are used to define the beam footprint on a horizontally diffracting monochromator, DCM1, so that the central portion of the beam reflected from M1 will be illuminated on DCM1. DCM1 uses double Si(111) crystals to provide a fixed exit

condition to a horizontally focusing mirror M2. A very small offset value of 6 mm and a total y-travel distance of less than 1 mm will be used for DCM1, to ensure high mechanical stability. DCM1 will be cryogenically cooled using liquid nitrogen, in order to minimize the thermally induced figure errors. During the commissioning, the practicality of using the dynamical bending capability of M1 to compensate for the thermally induced slope error on both M1 and DCM1 will be explored. As will be demonstrated later, placing high-heat load optics, M1 and DCM1, in the horizontal reflection/diffraction geometry, minimizes the negative effects of thermally induced slope errors on the optical performance of the beamline. However, diffracting in the horizontal direction results in flux loss predominantly at low energies, due to the linear polarization of the incident x-rays in the horizontal plane. At 10 keV, the flux loss due to double horizontal diffraction is about 15%.

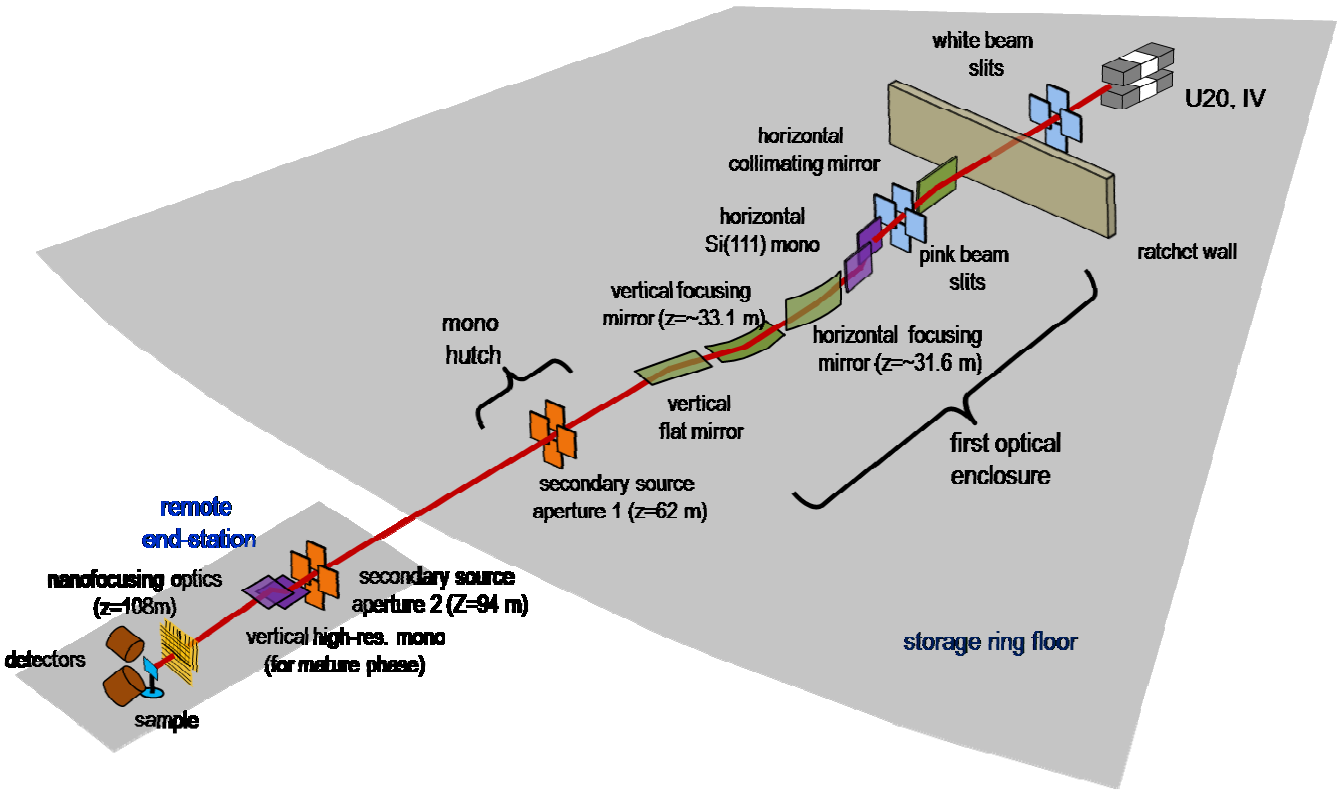

Figure 2.4.1. Overview of the major optical components of the HXN beamline. From the IVU20 undulator in the upper right corner, white beam slits (S1), horizontal collimating mirror (M1), pink beam slits (S2), horizontally diffracting Si(111) double crystal monochromator (DCM1), horizontal focusing mirror (M2), vertical focusing mirror (M3), vertical flat mirror (M4), secondary source aperture 1 (SSA1), secondary source aperture 2 (SSA2), vertically diffracting high-resolution double crystal monochromator (DCM2), and nanofocusing optics. DCM2 will be installed at the mature phase of the Beamline operation, when high-resolution nanofocusing optics requiring a higher degree of monochromaticity than Si(111) become available.

With a dynamic bending capability, a horizontally focusing mirror, M2, is used to image the source at two possible positions, in front of SSA1 (secondary source aperture 1) at z=62m or SSA2 (secondary source aperture 2) at z=94m. With the nanofocusing optics at z=108m, the secondary source at z=62m or z=94m results in an effective source-to-optic distance of 46m or 14m, respectively. Only one of the two secondary source apertures is used at a time. A larger distance between the secondary source to the nanofocusing optic is needed for a large focusing optic (>150 μm) or for coherently overfilling a smaller optic. More elaborate discussion on this topic will be presented in the following subsection.

A vertical mirror system, consisting of a focusing vertical mirror with bender (M3) and a flat vertical mirror (M4), is used to image the source in the vertical direction at the same position as the horizontal direction (i.e., either at z=62m or 94m). Rather than using a single focusing mirror, causing an angled trajectory of the x-ray beam, a double mirror system is considered. The two mirror system ensures an independent way to control focusing and positioning of the reflected beam, enabling a more straightforward method to implement a positional feedback system using beam position monitors.

The primary goal for the vertical mirror system is to maintain the same z-position for the secondary source in both the horizontal and vertical directions, completely eliminating astigmatism so that a two dimensional focusing optic such as Fresnel zoneplate can also be used without compromising its spatial resolution. For nanofocusing optical systems consisting of two 1D optics, such as MLLs, KB mirrors or Kinoform lenses, astigmatism is not important. By adopting different focal lengths in the horizontal and vertical directions, a common focal point can be achieved, even if the source-to-optic distances are different along the two directions. Nevertheless, it is important to maintain the compatibility for Fresnel zone plate optics, because low energy (< 10 keV) applications for the MLLs have not been demonstrated, to date.

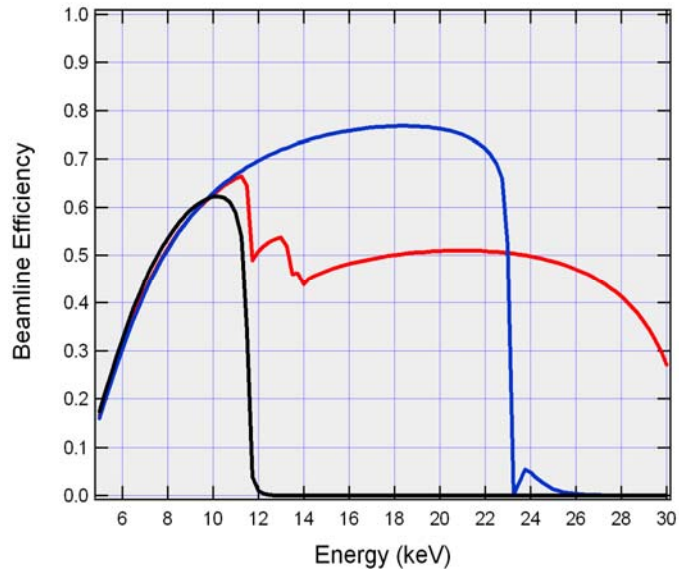

Figure 2.4.2: Beamline efficiency. The efficiency is calculated including the combined reflectivity of four mirrors, polarization due to the horizontally diffracting double-bounced Si(111) monochromators and the x-ray transmission through 1mm-thick Be. Three curves corresponds to different mirror surfaces: Si (black), Rh (blue) and Pt (red). The Beamline efficiency is better than 50% over most of its operating energies, 6-25 keV. The suppression of the beamline efficiency at low energies is primarily due to the polarization.

In order to provide effective rejection of high-order undulator harmonics, two different methods are possible: adjusting the incidence angle of M1 and M2 or implementing multiple cut-off energies at a fixed angle with different metal coatings on the silicon mirrors. Since M1 and M2 are physically separated, it is impossible to rotate them together. Thus, the conceptual design proposes to use three different reflecting surfaces, Si, Rh, and Pt, for all the mirrors with a fixed incidence angle of 2.7 mrad, to ensure adequate harmonic rejection and sufficient beamline efficiency over the operating energy of 6-25 keV. A fixed incidence angle for all the mirrors would also lead to more straightforward beamline alignment and diagnostics. Figure 2.4.2 shows the overall beamline efficiency vs. x-ray energy, taking into account the reflectivity of four mirrors, intensity reduction due to the polarization effect, and x-ray transmission through 1mm of Be windows. Except for narrow energy ranges, 6-7.5 keV and 24-25 keV, the beamline efficiency is better than 50%. The reduced efficiency at 6-7.5 keV is due to the horizontally diffracting monochromator, and lower efficiency of a Pt coating over a Rh coating is due to the multiple Pt L-edges.

The major optical components from the horizontal collimating mirror (M1) to the vertical flat mirror (M4) are housed in the FOE, while the monochromatic hutch houses the secondary source aperture 1 (SSA1). The most salient aspect of the HXN conceptual design is the endstation located within a separate HXN satellite building. The HXN endstation will house the secondary source aperture 2 (SSA2), high-resolution monochromator (DCM2), in addition to the HXN microscope.

The high-resolution monochromator, DCM2, will be implemented in the mature operating phase of the HXN when MLLs requiring a higher spectral bandwidth than that of Si(111) become available. The monochromaticity requirement states that the total number of zones of a MLL should be less than E/dE. This requirement translates into a lateral dimension smaller than 30 μm for a MLL with Δr = 1nm at 10keV or 150 μm for a MLL with Δr = 5nm. The monochromaticity requirement for a Fresnel zone plate is the same. The high resolution monochromator will consist of vertically diffracting double Si crystals with a higher index plane (i.e., 311 or 331). The selection of the spectral width for the high resolution monochromator will be based on the progress of the 1nm x-ray optics R&D.

2.4.2 Beamline Components in the First Optical Enclosure

Figure 2.4.3 shows the important beamline components in the FOE. Though specifically shown in the CAD drawings, some of the components such as gate valves, bellows, and transport pipes will not be described here. A diagnostic chamber (labeled as A) is to provide a future place holder for diagnostic elements such as an additional beam position monitor to increase the accuracy of the monitors in the FE. A white beam filter (labeled as B) is designed to house multiple x-ray absorbers. Some of the candidate materials are thin CVD diamond, Si, graphite and aluminum. The horizontal collimating mirror, M1, (labeled as C) collimates the incident x-rays to eliminate energy dispersion of the x-rays diffracted from the horizontal monochromator, DCM1 (labeled as G). A Bremsstrahlung collimator (labeled as D) and Bremsstrahlung stop (labeled as L) prevent unwanted radiation from passing down the beamline. A diagnostic chamber (labeled as H) immediately downstream of the horizontal monochromator can house both screen monitor and parasitic beam position monitor that can be used as feedback on the angle of the second crystal for DCM1. The horizontal focusing mirror, M2, (labeled as I) is used to image the primary source in front of either the secondary source aperture 1 (SSA1) or secondary source aperture 2 (SSA2). Mono beam position monitors (labeled as J and M) can operate parasitically to provide a feedback signal for correcting the drift of the mirrors and monochromator. A vertical mirror chamber (labeled as K) houses both focusing and flat mirrors. A mono shutter (labeled as N) provides the safety function for allowing safe entry into the mono hutch downstream of the FOE. The FOE is purposely designed to have some spare space. This will allow the possibility of future modifications or improvements of the beamline.

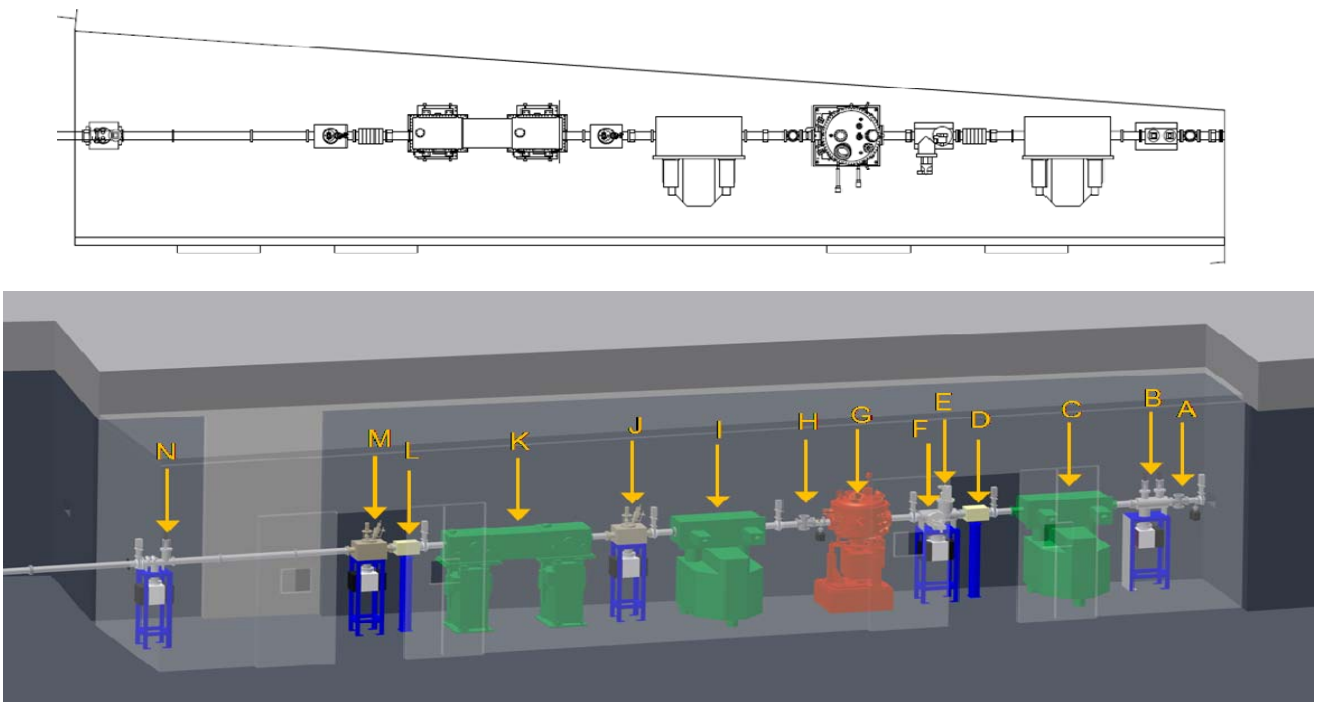

Figure 2.4.3. Planar (top) and 3D perspective (bottom) view of the first optical enclosure (FOE) and its major beamline components. A: diagnostic chamber. B: white beam filters. C: horizontal collimating mirror. D: Bremsstrahlung collimator. E: pink beam slits. F: pink beam screen monitor. G: horizontal monochromator. H: diagnostic chamber. I: horizontal focusing mirror. J: mono beam position monitor. K: vertical mirror chamber containing focusing and flat mirrors. L: Bremsstrahlung stop. M: mono beam position monitor. N: mono beam shutter. The white beam slits are located in the front end (FE).

2.4.3 Beamline Components in the Monochromatic Hutch

The monochromatic hutch houses the secondary source aperture 1 (SSA1) located at 62m from the source, as shown in Figure 2.4. It also provides 3m of space between the two Be windows (labeled as A and B). The monochromatic hutch will be used for commissioning of the FOE optics and for instrumentation development for stabilizing the beam through active feedback using the multiple parasitic beam position monitors, which are critical tasks for achieving the highest possible performance of the HXN beamline. To pass the beam to the endstation, a transport pipe will be connected between the two Be windows and evacuated the pipe. The mono beam shutter

(labeled as E) ensures safe entry into the endstation, even when monochromatic x-rays are in the monochromatic hutch. During the mature operation phase, if necessary, these two Be windows could be removed, and a permanent vacuum transport pipe can be installed, in order to reduce the x-ray absorption at low energies. To ensure a better use of the space, the hutch door will be installed on the right side of the hutch wall when looking downstream (i.e., the inboard direction).

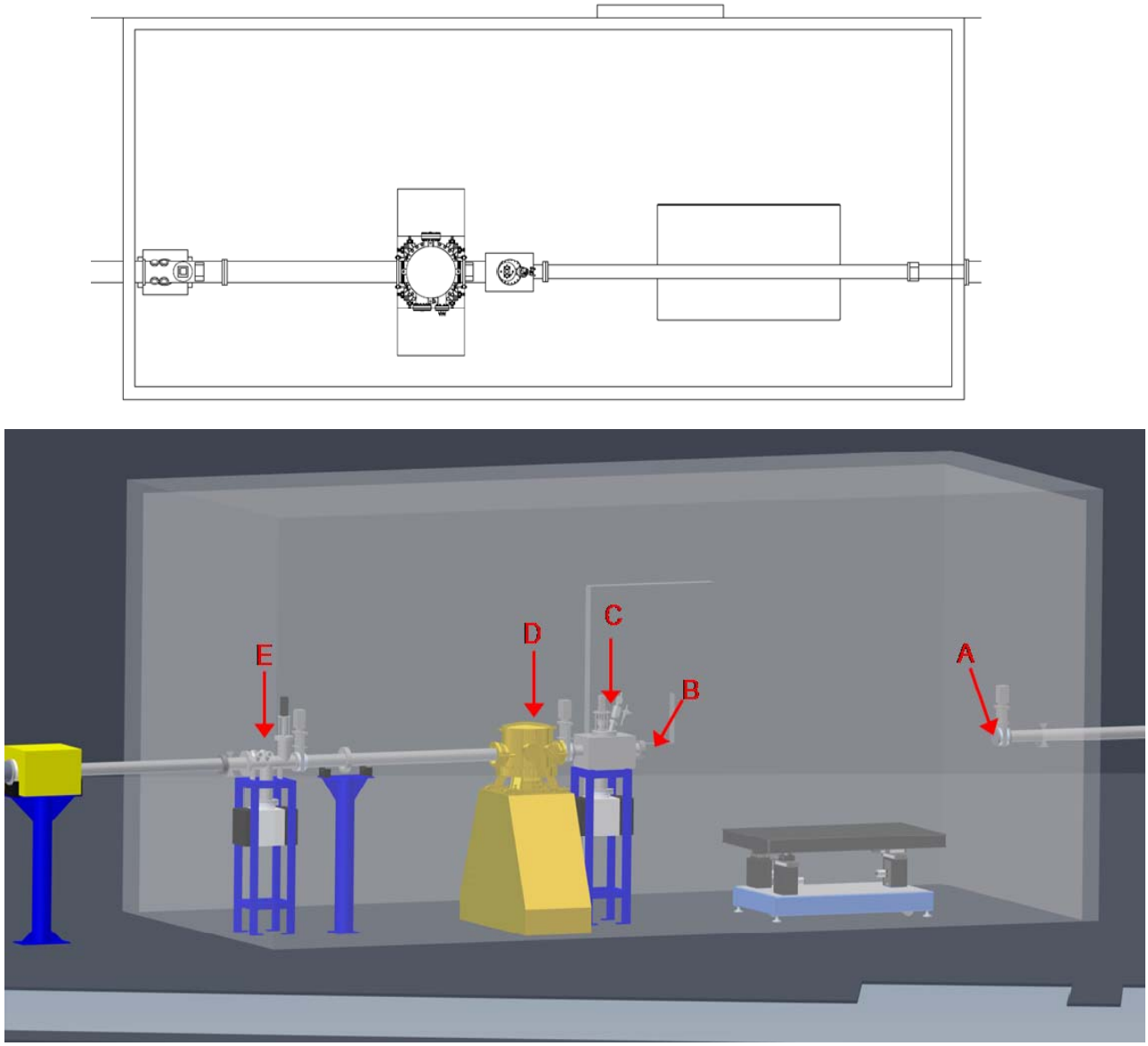

Figure 2.4.4. Planar (top) and 3D perspective (bottom) view of the monochromatic hutch and its major beamline components. A: Be window, B: Be window. C: mono beam position monitor., D: secondary source aperture 1 (SSA1). E: mono beam shutter. The monochromatic hutch will be used for commissioning of the FOE optics and instrumentation development for beam stabilization using multiple beam position monitors. To pass beam to the endstation, a vacuum pipe will be connected between two Be windows. During the mature operation phase, these two Be windows could be removed and a permanent vacuum transport pipe can be installed, in order to reduce the x-ray absorption at low energies.

2.4.4 Beamline Components in the Endstation and Satellite Building

The HXN endstation is physically separated from the storage ring building and the nearby LOB, in order to damp out the ambient vibrations originating from multiple sources. A HXN satellite workshop was held in June, 2009,

identifying the requirement for vibration and temperature stability, which is summarized in section 4. In order to maximize the structural filtering of the ground vibration at low frequencies (<10 Hz), the HXN satellite building will have a single large concrete slab with 1m-thickness under both endstation and user area, as shown in Figure 2.4.5.

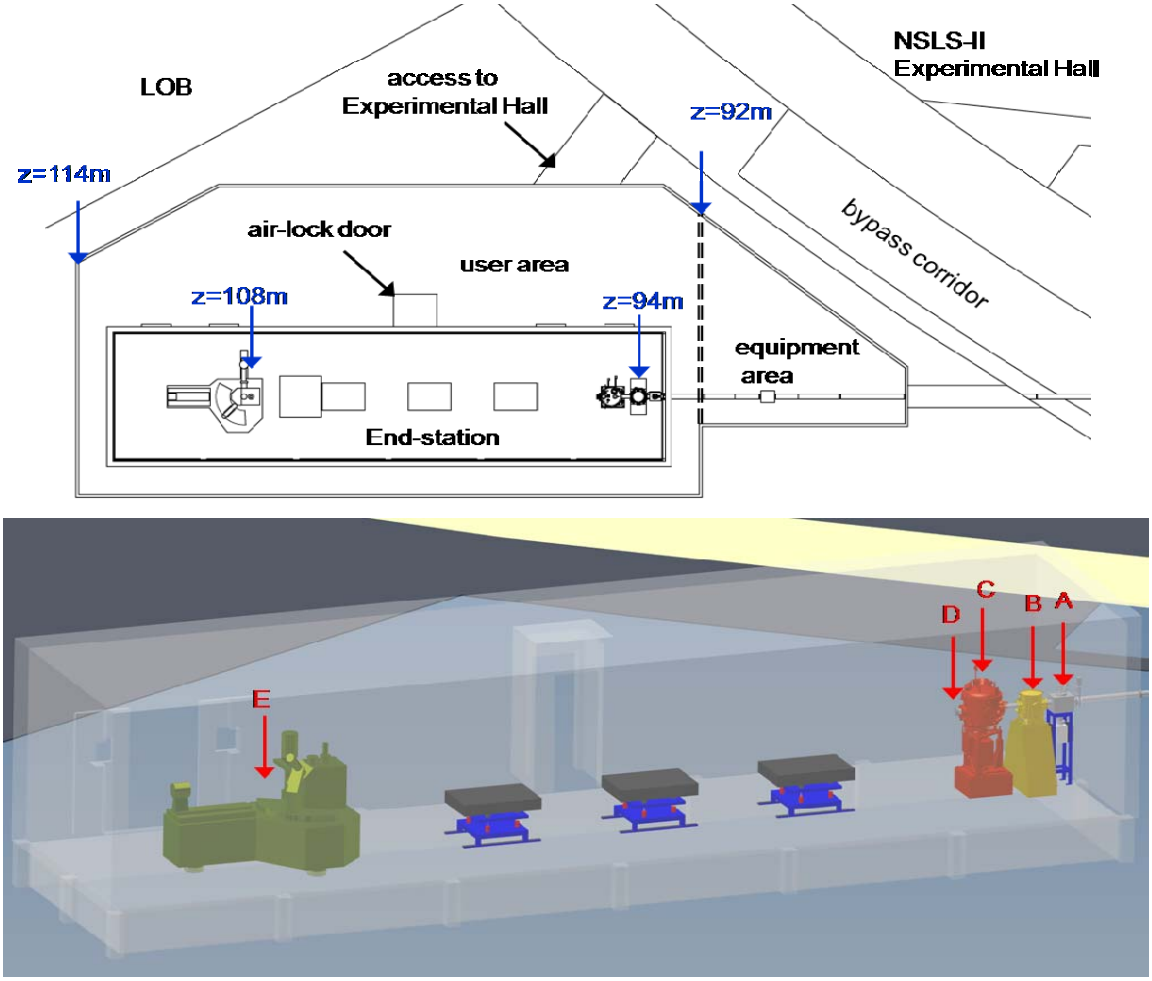

Figure 2.4.5. Planar (top) and 3D perspective (bottom) view of the endstation and its major beamline components. A: mono beam position monitor. B: secondary source aperture 2 (SSA2). C: high-resolution monochromator (to be installed in the mature phase). D: Be window. E: HXN microscope. The planar view shows a tentative satellite building floor. The satellite building will be in the corner between the NSLS-II storage ring building and the LOB. The endstation and user area will share the common concrete floor; the equipment area will have a separate concrete floor to prevent transmission of vibration and acoustic noise to the microscope. A connection to the experimental hall will be made in the upper right corner.

The beamline equipment, generating acoustic vibration and heat, will be located in the equipment area on a separate concrete slab. The utilities will be fed from the LOB with proper vibration isolation. The HXN satellite building is accessed from the bypass corridor of the experimental hall. The beam transport pipe from the experimental hall will be running through a short intermediate enclosure before entering into the satellite building. The floor structure of the satellite building shown in Figure 2.4.5 is a tentative layout. The final layout is currently under discussion.

The HXN endstation wall will be constructed with 8-inch concrete walls rather than steel walls. Concrete has superior vibration and acoustic damping properties and also provides better temperature stability, acting as a large thermal reservoir. The HXN endstation will have an air-lock entry consisting of two doors, in order to minimize the exchange of air, leading to potential temperature changes in the endstation. The dimension of the endstation will be 20m-long, 5m-wide and 3.5m-high. A one-foot deep trench with about 1 inch width will be cut outside of the endstation wall, so that high frequency noise (generated by users and computers) traveling near the surface will be scattered off by the trench and not transmitted into the endstation.

The endstation houses a mono beam position monitor (labeled as A), secondary source aperture 2 (SSA2, labelled as B), high-resolution monochromator (DCM2, labelled as C), exit Be window (labeled as D) and the HXN microscope (labeled as E). The microscope shown in the CAD drawing is a "mock" solid model taken from the nanoprobe instrument at 26-ID of the Advanced Photon Source. The design of the HXN microscope has not been carried out yet. This mock model is only for the visual purpose.

The HXN endstation length requirement of 20m is based on the need to ensure sufficient distance from the SSA2 to the nanofocusing optic. The conceptual design proposes a 14m distance. In addition, sufficient space (~5m) is needed at the downstream end of the nanofocusing optic, in order to provide space for microscope enclosure and detectors. Detectors for diffraction will be mounted on a separate granite table, isolated from the HXN microscope so that the movement of a large detector (up to a few kilograms) would not induce unwanted motions in the HXN microscope. Since an isolated satellite building will be constructed around the endstation, the dimension of the hutch must be sufficiently large to avoid a potential future need for additional space, which cannot be obtained without prohibitively expensive construction cost. Furthermore, a large interior dimension, proposed by the conceptual design, is extremely beneficial to retain a sufficiently large thermal reservoir, so that small fluctuations of local temperature due to turbulent air-flow from the ventilation system or exchanged volume of air due to entry or exit from the endstation does not influence the overall temperature stability in the endstation.

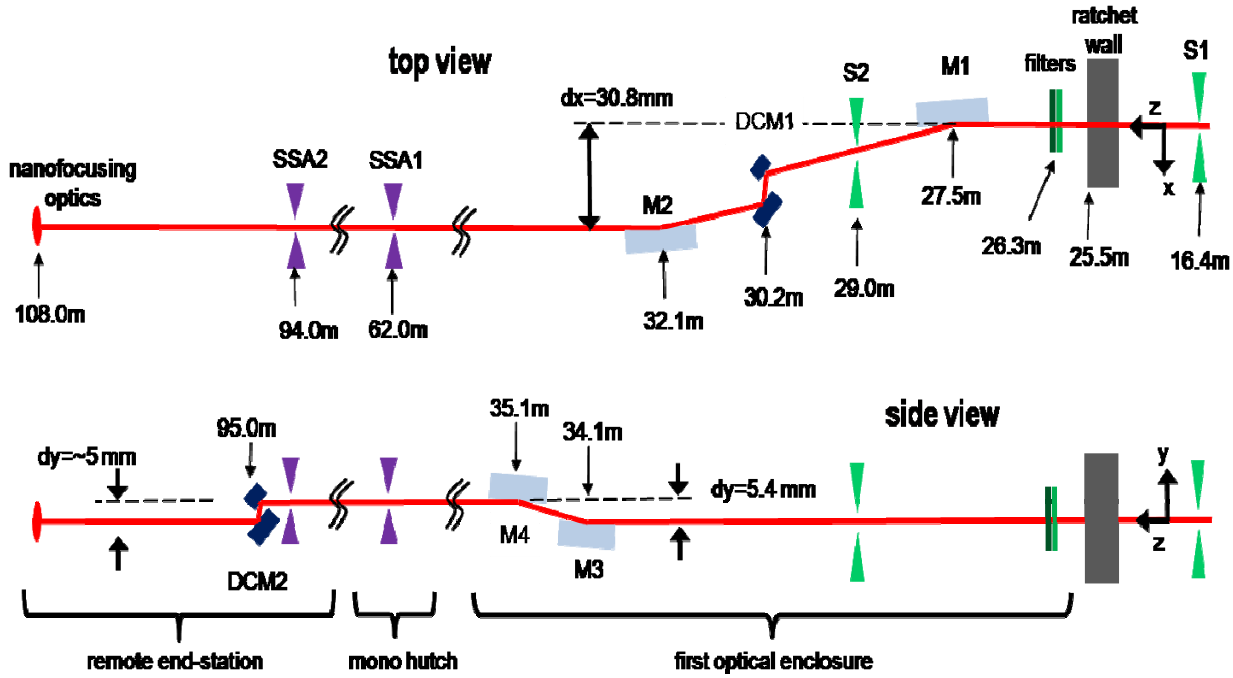

Figure 2.4.6. X-ray beam path through the major optical components of the HXN beamline. Top view shows the horizontal direction and side view the vertical direction. The coordinates are defined such that z-direction is along the beam, y-direction is up, and x-direction is the outboard direction. All the mirrors have the nominal incidence angle of 2.7mrad. The nominal offset distance for DCM1 is 6mm. The horizontal and vertical offsets are due to the reflection from the mirrors and monochromator.

<u>X-ray Beam Path through the HXN Optical Components</u>

Figure 2.4.6 shows the overall x-ray beam path through the HXN optical components. All of the optical components shown in Figure 2.4.6 have been already explained in the previous subsections. The coordinate system, adopted in this report, uses the same convention as the Advanced Photon Source, where z-direction is along the x-ray beam, y-direction is up, and x-direction is along the outboard or outward direction from the interior of the storage ring. In the horizontal direction, white beam slits, S1, limit the angular size of the incident beam onto the horizontal collimating mirror. With a nominal incidence angle of 2.7mrad at its center, M1 reflects the incident beam in the outboard direction. Pink beam slits, S2, limit the illuminated power onto the horizontal monochromator, DCM1. DCM1 operates at a fixed exit condition to position the beam onto the center of the horizontal focusing mirror, M2. M2 reflects the beam so that the central trajectory of the focused beam is parallel with the beam from the undulator. A separation distance of 4.6 m between M1 and M2 results in a horizontal offset

of 24.8mm. DCM1 adds a 6-mm offset in the same direction, resulting in a total horizontal offset of 30.8 mm. The first crystal of DCM1 diffracts in the same orientation as M1 (i.e., ++ geometry) in order to maximize the horizontal offset. A total offset of 30.8 mm is adequate for providing sufficient room for white beam Bremsstrahlung stop, which will be placed immediately outside of the DCM1.

In the vertical direction, the vertical focusing mirror, M3 (0.8m-long), reflects x-rays upward and the vertical flat mirror, M4 (0.8m-long), reflects the beam in a trajectory parallel with the x-ray beam from the undulator. A separation distance of 1 m between M3 and M4 results in a vertical offset of 5.4mm. When implemented in the future, the high-resolution monochromator, DCM2, located in the endstation will provide about a 5mm vertical offset in the opposite direction. During the initial operation phase, a total vertical offset of 5.4 mm will be used.

Beamline Operation Modes

There are three different possible operation modes for the HXN beamline, as schematically illustrated in Figure 2.4.7. In the diagram, a focusing mirror is represented as a lens. In this representation, the other optical components, such as monochromators and flat mirrors, are ignored because they do not manipulate the phase space of the beam. The three possible modes are high-coherence mode, high-throughput mode, and astigmatic high-coherence mode, distinguished by the location of the secondary source in the horizontal and vertical directions.

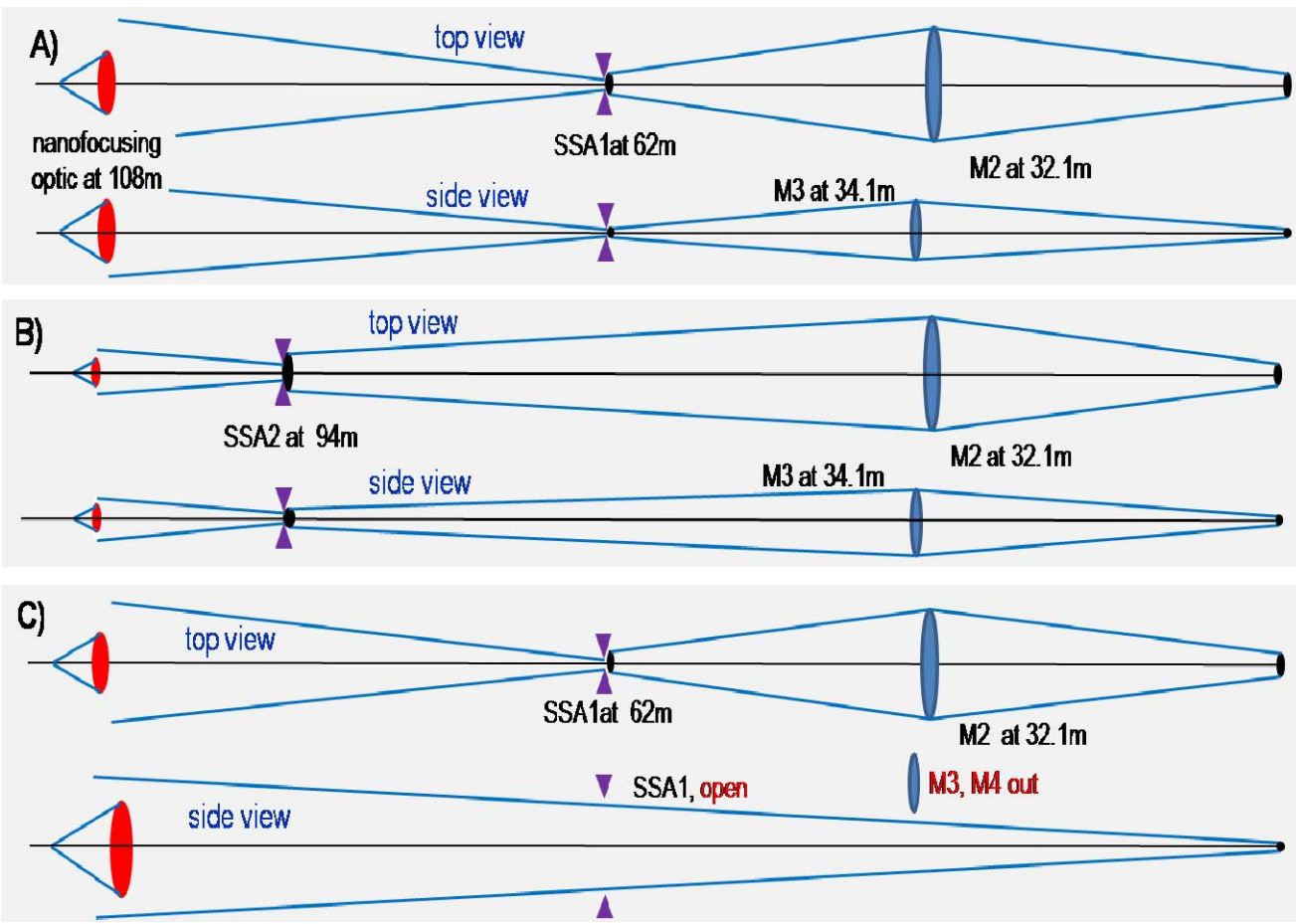

Figure 2.4.7:. Three possible operation modes for the HXN beamline. A) High-coherence mode, where the primary source from IVU20 is imaged in front of SSA1 at z=62 m by M2 (horizontal focusing mirror) and M3 (vertical focusing mirror), resulting in an effective source-to-focusing optic distance of 46 m. B) High-throughput mode, where the primary source is imaged in front of SSA2 at z=94 m, resulting in an effective source-to-focusing optic distance of 14m. C) Astigmatic high-coherence mode, where the secondary source at 62 m is used in the horizontal direction and the primary source s used in the vertical direction after moving M3 and M4 out of the beam. The beamline operation in astigmatic high-coherence mode requires lowering the vertical position of a few optical components by 5.4 mm.

High-Coherence Mode

In this mode, the x-ray source from IVU20 (this will be referred as the "primary source") is imaged in front of SSA1, located at 62 m by M2 in the horizontal direction and by M3 in the vertical direction. This geometric configuration corresponds to horizontal and vertical magnification factors of 0.93 and 0.82, respectively. At 10keV, the FWHM size of the secondary source would be 9.5 μm in the vertical direction and 94.1 μm in the horizontal direction if each mirror behaves as an ideal lens. Since the secondary source is much larger in the horizontal direction, a rather broad range of the aperture size can be selected in the horizontal direction. In order to prevent a possible source motion induced by thermal drift in the monochromator or mirrors, the secondary source aperture should not be set much larger than the FWHM size of the secondary source. This limits the range of the horizontal aperture up to about 100 μm and the vertical aperture up to about 10 μm. The low limit of the aperture depends on the quality of the polished blade of the aperture and the mechanical vibrations. A lower limit of 5 μm is expected to be feasible.

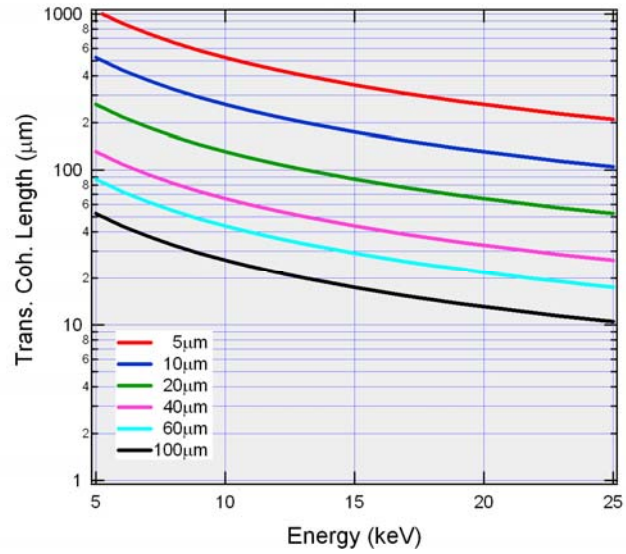

Figure 2.4.8: Transverse coherence length as a function of secondary source aperture size in high-coherence mode. The expected secondary source size at 10keV, imaged by the focusing mirrors, is 9.5 um (vertical) and 94.1 um (horizontal) in FWHM. In order to prevent source motion, the secondary source aperture should not be opened more than the FWHM beam size. Consequently, the range of aperture sizes is rather limited in the vertical direction.

A practical criterion for coherent illumination is to ensure that the transverse coherence length is larger the lateral size of the nanofocusing optic. Figure 2.4.8 shows the FWHM transverse coherence length as a function of the size of the secondary source at z = 62 m. In order to achieve a diffraction limited focus size, a nanofocusing optic must

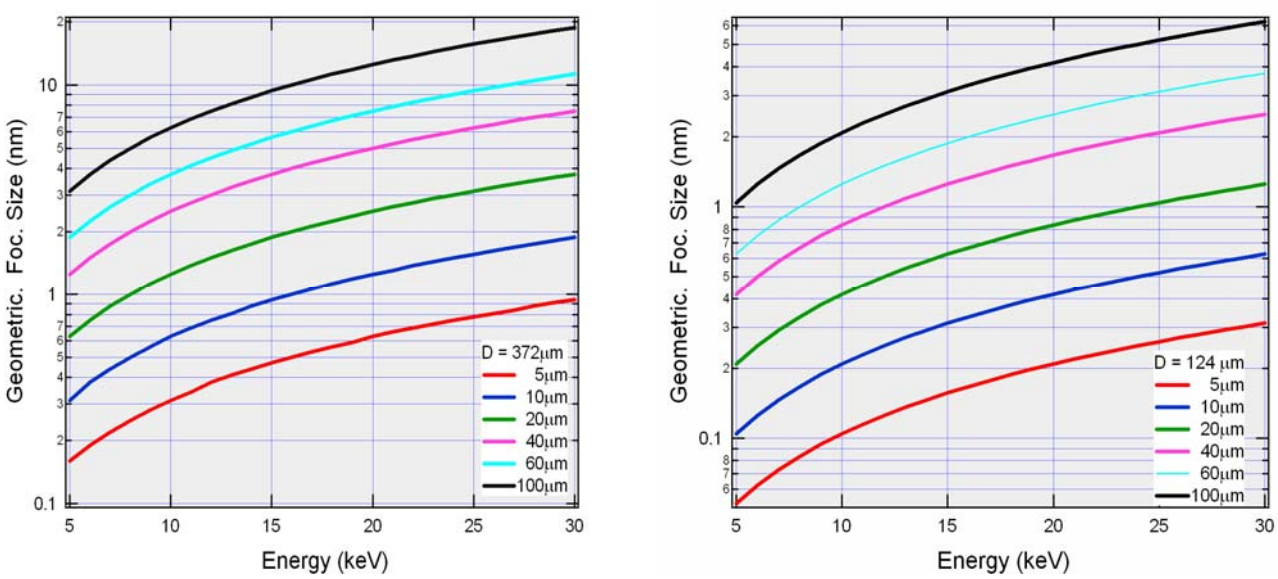

Figure 2.4.9: Expected geometric focus size based on demagnification of the secondary source size by the nanofocusing optic in high-coherence mode. Two cases are considered. A) MLL optic with a lateral dimension, D=372 μm and Δr =1nm (a focal length of 3 mm at 10keV) and B) D=124 μm and Δr =1nm (a focal length of 3mm at 10keV).

be illuminated coherently. At 10 keV, an aperture size from 5 to 100 μm produces a transverse coherence length from 500 to 25μm, respectively. However, in the vertical direction, the range of the transverse coherence length is

limited to between 250 to 500 μm, because the secondary source size is quite small in the vertical direction. Since the transverse coherence length is linear with the x-ray wavelength, the expected transverse coherence length is reduced by 50% for the same aperture size at 20 keV. A large transverse coherence length up to 500 μm is ideal for nanofocusing optics with a large lateral dimension. For example, a pair of KB mirrors with a sufficiently large working distance could be accommodated. However, for other types of nanofocusing optics such as MLLs and FZPs, fabricating a large lateral dimension is technically challenging. For example, fabricating MLL optics with a size larger than 100 μm has not been achieved, yet. The current goal of the NSLS-II 1nm x-ray optics R&D is to achieve a lateral dimension of 100~150 μm. Therefore, a considerable fraction of the coherent flux would be wasted in the vertical direction if the lateral size of MLLs or FZP is less than 250 μm.

To ensure that the proposed optical scheme can provide sufficient conditions for a 1nm focal spot, expected geometrical focal sizes are calculated for two hypothetical cases: for a MLL optic with a lateral dimension D=374 μm with the outmost zone width Δr=1nm, and for a MLL optic with D=124 μm and Δr=1nm. At 10 keV, the first MLL optic has a focal length of 3 mm, and the second optic, 1 mm. The two plots in Figure 2.4.9 show the estimated geometric focus sizes based on the demagnification factors considering a 46m-distance from the secondary source to the nanofocusing optics and their energy-dependent focal lengths. For a MLL optic with D=374 μm, a SSA size of 5 μm meets the necessary condition to achieve a 1nm focus size over the operational energy range of the HXN beamline. A SSA size of 10 μm meets the requirement up to 15 keV. For a MLL optic. In summary, the high-coherence mode can deliver a transverse coherence length up to 500 μm at 10 keV. In with D=124 μm, the 1nm requirement is met for 5~40 μm SSA sizes over most of the operating energies. The same conclusion is also valid for other nanofocusing optics.

In summary, the high-coherence mode can deliver a transverse coherence length up to 500 μm at 10 keV. In addition, it provides sufficient source-demagnification for 1nm focusing, for a nanofocusing optic with a lateral size of up to ~400 μm over the entire operational energy range. On the other hand, this mode can lead to loss of coherent flux if the size of the optic is smaller than ~250 μm.

High-Throughput Mode

In the high-throughput mode, the primary source is imaged in front of SSA2 located at z = 94 m, with a magnification factor of 1.76 in the vertical direction and 1.93 in the horizontal direction. Consequently, the expected secondary source size is 21.1 and 193.9 μm in the vertical and horizontal directions, respectively. With only a 14m distance from the secondary source to the nanofocusing optic, the transverse coherence lengths produced in this optical scheme are much smaller than those in high-coherence mode. Figure 2.4.10 shows the achievable transverse coherence length as a function of the secondary source aperture size. With an aperture size of 10 μm, the transverse coherence length at the plane of the nanofocusing optic is 75 μm at 10 keV. With an aperture size of 5 μm, a transverse coherence length of 150 μm can be achieved at 10 keV. Consequently, a small nanofocusing optic (<150 μm) can be coherently illuminated in this mode.

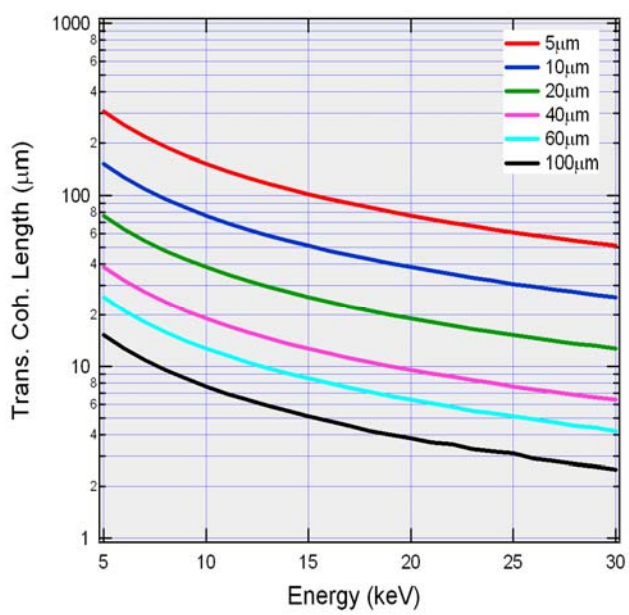

Figure 2.4.10: Transverse coherence length as a function of secondary source aperture size and x-ray energy in high-throughput mode.

The greatest utility of this mode is to achieve higher integrated flux over the focus spot by relaxing the diffraction-limited condition. In this way, spatial resolution can be traded with flux conveniently without moving the nanofocusing optic. Since the vertical size of the secondary source is 21.1μm, the range of the vertical aperture size is wider than in high-coherence mode.

Astigmatic High-Coherence Mode

In astigmatic high-coherence mode, the vertical mirrors are moved out of the beam, so that the nanofocusing optic is looking at the primary source in the vertical direction. The horizontal mirrors are still in place, creating a secondary source in front of SSA1 at 62 m from the primary source. The vertical transverse length at 10 keV is 508 μm, good for a large-size nanofocusing optic. With the vertical mirrors out of the beam, there is no optical element in the vertical direction. The source stability is unaffected, to the first degree, by the thermal drift or mechanical vibration of the beamline optics. Since the distance from the source to the nanofocusing optic is drastically different between the vertical and horizontal direction, this mode is not suited for FZPs. This mode is best utilized by a pair of KB mirrors. Unlike the MLLs, two KB mirrors must be separated by at least the length of the mirror, so that the horizontal and vertical focal lengths can differ by almost a factor of two if the same mirror length is used.
In the astigmatic high-coherence mode, the source-to-optic distance differs by almost a factor of two between the horizontal and vertical direction, providing a natural fit to nanofocusing KB mirrors. Since running the beamline in astigmatic high-coherence mode requires adjustment of the vertical position of both SSA2 and the HXN microscope, switching over to this mode of operation cannot be carried out as routinely as switching between the other two modes.

Implementing high-resolution MLLs with sufficient lateral sizes (for example, D>30μm and Δr=1nm, or D>150μm and Δr=5nm) requires a high resolution monochromator with a smaller energy band than that of the Si(111) monochromator, in order to satisfy monochromaticity requirements. A high resolution monochromator with a smaller angular acceptance can be accommodated without significant flux loss if the vertically focusing mirror, M3, is used to collimate the x-ray beam vertically. This is a variation of the astigmatic high-coherence mode described above but with M3 and M4 still in the beam. In addition, the vertical collimation helps minimize significant overfilling of the vertical transverse coherence length onto the MLL optics, in case the size of the MLL is moderately large (D~100μm). Since implementation of this mode of operation will take place after significant advance in the 1nm optics R&D, this CDR report will not elaborate further, other than stating that the current conceptual design accommodates the use of high resolution MLLs without significant flux loss. Table 2.4.1 summarizes all three possible modes of the operation:

Table 2.4.1. Summary of Three Possible Operational Modes.

Operation Modes	Source Position		Optical Components Used	Applications
	Hor.	Vert.		
High-coherence	z=6 m	z=62 m	M1, M2, M3, M4, SSA1	Diffraction-limited focusing of MLL, FZP, Kinoform or KB of lateral size up to 500 μm.
High throughput	z=94 m	z=94 m	M1, M2, M3, M4, SSA2	Diffraction-limited focusing of small (<150um) MLL or partially-coherent illumination of larger MLLs or ZP for higher focused flux.
Astigmatic high-coherence	z=62 m	z=0 m	M1, M2, SSA1	Diffraction-limited focusing of KBs with a maximum working distance.

Expected Optical Performance

Previous subsections elaborated on how to configure the HXN optical components to manipulate the transverse coherence length to match the lateral size of a nanofocusing optic that will be used for x-ray microscopy experiments. When the FWHM transverse coherence is exactly matched to a lateral dimension of a nanofocusing optic, the focusing optic accepts 76% of the coherent flux present at the plane of the focusing optic. 76% corresponds to the integral of a Gaussian curve over its FWHM. Under this condition, a nanofocusing system consisting of two linear optics such as MLLs or KBs accepts 57.9% of the available coherent flux. If the nanofocusing optic is smaller than the transverse coherence length, it accepts a smaller fraction of the coherent flux. For example, in high-coherence mode, a MLL with a lateral size of 100 μm is placed in the beam at z=108 m; the horizontal coherence length can be matched by adjusting the horizontal size of the SSA. However, in the vertical direction, the secondary source size is already much smaller than the required aperture size. Consequently, a sizable fraction of the coherent flux cannot be accepted by the nanofocusing optic. Table 2.4.2 summarizes the fraction of the coherent flux that can be accepted by nanofocusing optics with different lateral sizes.

Table 2.4.2. Fraction of the Coherent Flux Accepted by Nanofocusing Optics.

	High-Coherence Mode				High-Throughput Mode			
	at 10 keV		at 20 keV		at 10 keV		at 20 keV	
Size of focusing optic (μm)	% coh. flux accepted by focusing optic	Required SSA size (μm)	% coh. flux accepted by focusing optic	Required SSA size (μm)	% coh. flux accepted by focusing optic	Required SSA size (μm)	% coh. flux accepted by focusing optic	Required SSA size (μm)
50	13.9	50.2	27.0	25.1	57.9	13.1	62.3	6.5
100	27.0	25.1	48.9	12.5	57.9	6.5	63.3	3.2
150	38.8	16.7	57.9	8.4	57.9	4.4	57.9	2.2
200	48.9	12.5	57.9	6.3	57.9	2.2	57.9	1.6
300	57.9	8.3	57.9	4.2	57.9	2.5	57.9	1.1
400	57.9	6.3	57.9	3.1	57.9	1.6	57.9	0.8
500	57.9	5.0	57.9	2.5	57.9	1.3	57.9	0.7

The required SSA size matches the FWHM transverse coherence length to the lateral size of the nanofocusing optic. This will serve as a reference point for designing an experiment. In practice, the size of the SSA can be smaller or larger, depending on the need for more flux or more coherent illumination. In high-coherence mode, a monotonic decrease in the fraction of the accepted coherent flux with decreasing size of the nanofocusing optic is due to the fact that the vertical SSA cannot be opened further. In other words, the nanofocusing optic is becoming over coherently illuminated. The cases, requiring a SSA size less than 5 μm, are marked in light gray, indicating that these values may be hard to achieve. The feasibility to maintain aperture sizes below 5 μm needs to be explored during the beamline commissioning period. In high-throughput mode, nanofocusing optics with sizes larger than 150 μm are not feasible to use because the FWHM vertical source divergence is less than the angular size of the optics, leading to non-uniform illumination of the focusing optic.

It is important to note that all the calculations shown so far are based on ideal beamline optics free from figure errors. Since all x-ray mirrors have figure errors, the effect of figure errors must be pointed out. In the first approximation, the figure errors broaden the effective size of the secondary source. Since the vertical source size is more than 8 times smaller than the horizontal source size, the effect of figure errors is much more pronounced in the vertical direction. For example, in high-coherence mode, a combined 0.2 μrad figure error results in 50% broadening of the secondary source size in the vertical direction. On the other hand, the same figure error results in less than 1% broadening in the horizontal direction. Figure errors on the x-ray mirror are not likely to produce smooth intensity broadening of the secondary source. Consequently, the broadening of the secondary source size does not immediately translate in the ability to open up the secondary source aperture size. In this case, the secondary source aperture also works as a spatial filter to cut out the irregular part of the beam.

The broadening of the secondary source size due to the figure error results in the loss of the integrated flux through the secondary source aperture because some of the x-rays are channelled away from the central optical axis. Figure 2.4.11 shows the fraction of the flux loss due to the combined figure error in the case when the secondary source aperture is set at 10 μm. In this estimation, the Gaussian distribution is used for the secondary source broadening due to the figure errors, and the intensity loss in the central optical axis was calculated. The total figure error is the combined figure errors for the two mirrors in each direction. For the horizontal direction, a total figure error of 1μrad results in less than 10% loss of the integrated flux. On the other hand, in the vertical direction a total figure error of 1μrad leads to about 60% loss of the flux, utilized by the nanofocusing optic. This estimate provides specifications on the figure error limit on the vertical mirrors. For example, a figure error less than 0.2 μrad is required to prevent the flux loss less than 20%.

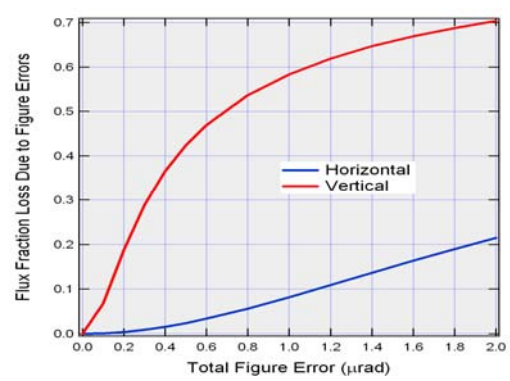

Figure 2.4.11: Effect of figure error. The fraction of the flux used for nanofocusing diminishes with increasing figure error from the beamline mirrors. The estimation shows the reduction of the integrated flux through 10 μm secondary source aperture as a function of the total figure error. The total figure error is the combined figure error due to all the mirrors in each direction. The effect of figure errors is much more dramatic for the vertical direction because the vertical source size is more than 8 times smaller than the horizontal source size. The relative impact is much larger even with

2.5 High Heatload Optics

Based on the design of the beamline optics, the power delivered to, transmitted from, and absorbed in a few key high heatload components is listed below. The calculation for the power distribution was carried out for K=1.83 corresponding to the minimum undulator gap of 5 mm and the fundamental undulator photon energy of ~1.6 keV, the condition generating the highest power output.

Table 2.5.1: Power on High Heatload Optics

Beamline component	Incident aperture size μrad (H x V)	Power delivered	Power absorbed	Power transmitted	Notes
Fixed mask	Unrestricted	~8kW	~2.4kW	~5.6kW	In the front end
White beam slits	500 x 300	~5.6kW	~5.42kW	180W	In the front end. Using an absorber can lower the incident power to M1.
Hor. col. mirror (M1)	80 x 40	180W	137W (Si) 68W (Rh) 27 W(Pt)	43W (Si) 112W(Rh) 153W(Pt)	2.7mrad incidence angle and Si, Rh, and Pt reflective surfaces. Pt coating reflects the highest power.
Si(111) mono (DCM1)	60 x 30	94W	94W	~0 W	153W is reduced to 94W by the pink beam slits (S2).

As summarized above, the power generated from the IVU20 undulator is significant but not unmanageable. By implementing incremental power reduction using the fixed mask and white beam slits, the total power delivered to the horizontal collimating mirror (M1) is about 180 W. This is an amount of power comparable to the APS undulator beamlines. The highest power loading condition for the mirror is at energies less than 11 keV, where a Si surface is used for harmonic rejection, leading to an estimated absorbed power of 137 W. On the other hand, the monochromator is exposed to the highest delivered power at energies above 23 keV, where a Pt surface is used for harmonic rejection. The illuminated aperture of the monochromator will be made smaller to reduce the delivered power to the monochromator and to reject the x-rays reflected from the region of the mirror with a high temperature gradient (i.e., edge of the beam). With an incident aperture of 60 x 30 μrad onto the monochromator, the maximum delivered power is 94 W.

Since ensuring proper management of the delivered power to the monochromator is of the utmost importance, finite element analysis (FEA) studies have been performed to quantify the amount of slope error induced by the incident x-rays. This conceptual design report summarizes the key finding in the FEA analysis. The FEA model was carried out using the following parameters:

- A Si(111) crystal, 50 mm long, 30 mm wide and 20 mm thick
- A horizontal diffraction geometry with an incidence angle of 14.04˚ corresponding the Bragg energy of 8.15 keV
- Cryogenically cooled with LN2 at 77K with a side cooling geometry with effective convection film coefficient values h_{conv}= 0.003 W/mm^2/K and h_{conv}= 0.005 W/mm^2/K, representing different effectiveness of thermal contact
- Power density corresponding to K=1.83, reflected from a Pt coating, which corresponds to the worst-case scenario in terms of delivered power density to the monochromator. This condition is met only at 24 keV but with an incidence angle of 9.48˚, resulting in 66% of the surface power density of the simulated condition

Three different angular aperture sizes were used to study the induced slope error as a function of different amounts of delivered power. The results of the FEA model are summarized in Table 2.5.1.

Table 2.5.2. Results of the FEA Analysis on horizontally diffracting Si(111) monochromator (DCM1).

Simulation #	Angular aperture H x V (μrad^2)	Power delivered	h_{conv} (W/mm^2)	Peak temp.	Min temp.	Induced slope error
1	44.4 x 22.2	53 W	0.003	98.9 K	86.5 K	4 μrad
2	66.6 x 33.3	105 W	0.003	116.5 K	95.5 K	1.2 μrad
3	88.8 x 44.4	201 W	0.003	150.0 K	109.0 K	36 μrad
4	44.2 x 22.2	53 W	0.005	94 K	82.6 K	4.6 μrad
5	66.6 x 33.3	105 W	0.005	105.8 K	88.05 K	4.8 μrad
6	88.8 x 44.4	201 W	0.005	127 K	96.1 K	4.8 μrad

As the incident energy decreases toward 6 keV, the increase in the Bragg angle is compensated by the decrease in the power density from the undulator. As the energy increases from 10 keV, the incidence angle decreases so that the power density on the surface decreases. Thus, the simulation shown here represents the worst case in terms of the power density on the monochromator surface. In all cases, a higher h_{conv} value leads to a lower peak temperature, indicating that more effective thermal contact leads to more efficient cooling. For a fixed h_{conv} value, a higher delivered power results in a higher peak temperature at the center of the beam footprint on the crystal, as expected. However, the induced slope error does not exhibit a linear relationship with respect to the delivered power or the peak temperature. This nonlinear behavior is due to the nonlinear thermal expansion coefficient of Si with temperature. In particular, near 120K, the thermal expansion coefficient of Si becomes zero. This is why simulation #6 (201W of power resulting in the peak temperature 127 K) produced the same slope error as simulation #5 (105 W of power resulting in the peak temperature 105.8 K). With the exception of simulation #3, all five cases resulted in a thermally induced slope error of less than 5 μrad. At 8 keV, the Darwin width of the Si(111) is 26.4 μrad, and a slope error less than 5 μrad is acceptable. During the actual operation of the HXN beamline, the power to the monochromator will not exceed 100 W.

Since the horizontally collimating mirror (M1) upstream of the Si(111) monochromator (DCM1) has a dynamic bending capability, it could be feasible to compensate the induced slope error on the monochromator and the collimating mirror itself by controlling the bending curvature of the collimating mirror. The practicality of this idea will be extensively explored during the commissioning of the beamline.

In the HXN conceptual design, the primary high heatload optics (the mirror and monochromator) are placed in the horizontal reflection/diffraction geometry. As mentioned in section 2.4, the optical performance degradation due to the figure errors is much less pronounced in the horizontal direction. Thus, the overall impact of the thermally

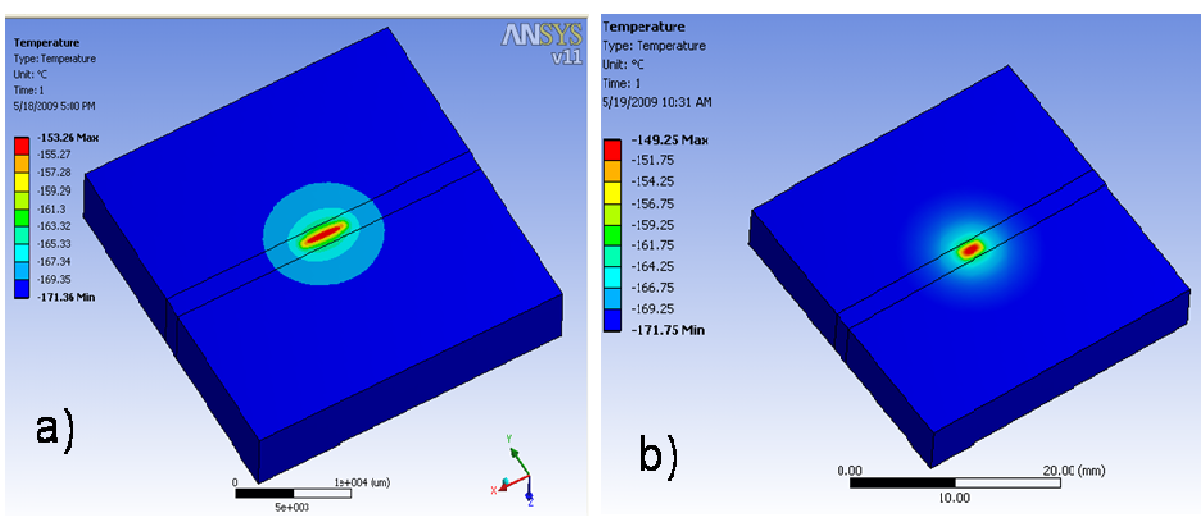

Figure 2.5.1: Comparison of the FEA simulated temperature distributions on the Si monochromator crystal placed in a) horizontal diffraction geometry and b) vertical diffraction geometry. With the identical incident angle, the horizontal diffraction geometry leads to a lower surface power density and consequently a lower peak temperature.

induced figure error is reduced by implementing a horizontal geometry. In addition, placing the high heatload optics in the horizontal geometry also results in reduction of the power density on the surface of the mirror and monochromator. Figure 2.5.1 shows the temperature distribution on a Si monochromator surface in two different diffraction geometries but under identical normal incident power. Because of the inherent asymmetry of the undulator source along the horizontal and vertical directions, the spread of the incident power density in the horizontal diffraction geometry leads to a lower power density on the surface, resulting in a lower peak temperature. For example, the FEA simulations shown in Figure 2.5.1 predicted a difference of 4 K in the peak temperature between the two cases.

In summary, the HXN utilizes incremental power management from the fixed mask to the monochromator. The initial FEA analysis indicates that the thermally induced slope error is less than 5 μrad. The FEA analysis also demonstrates that the horizontal diffraction geometry results in a smaller power density on the crystal surface. This conclusion is also applicable to the high heatload mirror.

2.6 List of Major Components

The major beamline components, along with their distance from the source, are listed in Tables 2.6.1 through 2.6.4. The HXN beamline plans to use the X–Y slits in the front end as its white beam slits. A more complete list is provided in section 8 (Appendix 2) of this report.

Table 2.6.1. Front End Components Used by the HXN Beamline.

Description	Symbol	Z (m)	Notes
White Beam Slits	S1	16.4	To limit the white beam onto M1

Table 2.6.2. Major Components in the HXN FOE. (Ratchet wall ends at 25.5 m. FOE ends at z=40.0 m.)

Description	Symbol	Z (m)	Notes
Aperture Plate	AP	25.7	~5 mm circular aperture to prevent accidental power overload to BL optics.
Diagnostic Chamber	DC1	25.9	for BL diagnostic
White Beam Filters	WBF	26.3	to provide different combination of x-ray absorbers
Be window	BW1	26.6	to isolate BL vacuum from FE
Horizontal Collimating Mirror	M1	27.5	water-cooled
Bremsstrahlung Collimator	CO	28.6	BL safety component
Pink Beam Slits	S2	29.0	to define incident illumination onto DCM1
Pink Beam Screen Monitor	PBSM	29.2	for BL diagnostic
Horizontal Double Crystal Monochromator	DCM1	30.2	Si(111), LN2-cooled
White beam Stop	WBS	30.7	placed outside of DCM1
Diagnostic Chamber	DC2	30.9	for BL diagnostic
Horizontal Focusing Mirror	M2	32.1	
Mono Beam Position Monitor	BPM1	33.3	parasitic beam position monitor
Vertical Focusing Mirror	M3	34.1	
Vertical Flat Mirror	M4	35.4	
Bremsstrahlung Stop	BS	36.3	BL safety component
Mono Beam Position Monitor	BPM2	36.8	parasitic beam position monitor
Mono Beam Shutter	MS1	39.5	BL safety component

Table 2.6.3. Major Beamline Components in the Monochromatic Hutch of the HXN Beamline.

Description	Symbol	Z (m)	Notes
Be window	BW2	58.0	to allow diagnostic experiments in the mono hutch
Be window	BW3	61.0	to allow diagnostic experiments in the mono hutch
Mono Beam Position Monitor	BPM3	61.3	parasitic beam position monitor
Secondary Source Aperture	SSA1	62.0	to define the secondary source size
Mono Beam Shutter	MS2	64.2	BL safety component

Table 2.6.4. Major Beamline Components in the HXN Endstation.

Description	Symbol	Z (m)	Notes
Mono Beam Position Monitor	BPM4	93.4	parasitic beam position monitor
Secondary Source Aperture	SSA2	94.0	to define the secondary source size
High-Resolution Monochromator	DCM2	95.0	To satisfy the monochromaticity condition for nanofocusing optic. To be installed in the mature phase.
Be Window	BW4	95.5	
HXN Microscope		108.0	The position of the focusing optic for the HXN Microscope

2.7 Summary of Beamline Performance Specifications

Spatial resolution

From 30nm down to the achievable resolution limit using a scanning x-ray microscopy. The ultimate spatial resolution is ~1nm.

Compatibility of different types of nanofocusing optics

Three different possible modes of operation ensure compatibility of all nanofocusing optics. At 10 keV, an aperture size up to 500 μm can be coherently illuminated using monochromatic x-rays.

X-ray energy range

From 6 keV to 25 keV. The lower energy range is limited by the horizontal polarization of the incident beam and the horizontal monochromator. The upper energy is tentative and will depend on the length and offset of the monochromator.

Techniques supported

- X-ray fluorescence
- Nanodiffraction
- Coherent diffraction imaging
- Differential phase-contrast imaging

Expected beamline efficiency through mirrors and monochromator

Approximately 50% for 8-22 keV

Targeted figure errors on mirrors

Vertical: less than 0.20 μrad through both mirrors, M3 and M4
Horizontal: less than 1.0 μrad through both mirrors, M1 and M2
Achieving figure below 0.5μrad is non-trivial and require intimate collaboration with the vendors.

Requirement on the slope error on monochromator induced by the power of the incident beam

Less than 20% of the Si(111) Darwin width at all energies

Targetted Beamline stability

The beam positioning feedback system must prevent loss of the intensity and the drift of the focused beam. The angular stability of the beam with an accuracy of 0.2 μrad or better is desired. The experimental methods for accurate beam positioning monitoring need to be developed during the commissioning period of the beamline.

Proposed utilization of coherent flux

Better than 50% of the coherent flux available from the source after accounting for the beamline efficiency and additional x-ray transmission due to the windows or possible air and helium path.

3 ENDSTATION INSTRUMENTATION

The most important endstation instruments are the HXN microscope with detectors and the HXN prototype. Based on the latest DOE review and inputs from the BAT, the overall strategy for constructing the HXN microscope has been recently modified. The recommendation is to design and construct an HXN microscope that can be used to carry out scientific investigations on "day 1" of the HXN operation. The primary function of the HXN microscope is to enable state-of-the-art x-ray microscopy experiments with comprehensive integration of the control system and the detector. On the other hand, the HXN prototype will be developed with a much higher level of positioning specification, in order to accommodate x-ray microscopy experiments with the highest spatial resolution down to the ultimate goal of ~1 nm. From an instrumentation point of view, combining the two capabilities into a single instrument is highly impractical, resulting in potential risks for productive scientific experiments. The HXN prototype will be developed under the Nanopositioning R&D, by incorporating the lastest advances in nanopositioning, vibration damping and advanced control feedback. Detailed design of the prototype will be finalized by FY2012 and a prototype will be constructed by end of FY2012. However, achieving its ultimate performance with subnanometer accurac may require a longer-term development beyond the initial commissioning of the HXN beamline. One the other hand, the HXN microscope will probably be constructed by a vendor through intimate interaction with the HXN team. Tentative requirements of the HXN microscope are listed below.

3.1 Key Requirements of the HXN Microscope

- Spatial resolution: from 30nm~10 nm
- The supported spatial resolution dictates not only the choices of the nanofocusing optics but also the accuracy of the positioning system. The current state-of-the-art x-ray microscopes have a positioning stability of 2~5 nm (rms). In order to accommodate the spatial resolution 30~10 nm, the HXN microscope requires a positioning/scanning accuracy of 1~2 nm.
- Short and longer term positioning stability: The HXN microscope is required to have short-term (~a few hours) and longer-term (~days) stability using close-loop differential positioning feedback between the optics and the sample.
- Fly-scan capability: A conventional method of "move, stop, and measure" imposes significant measurement overhead, because of the settling time required to stabilize on the final position with accuracy. The measurement should be carried out continuously while the sample is being scanned by adequate "hand-shake control" between the motion controller and the detectors.
- Supported techniques: x-ray fluorescence, nanodiffraction, coherent diffraction imaging, and differential phase-contrast imaging. Nanodiffraction requires a minimum of one rotation with the axial run-out error less than 1 μm.
- Supported nanofocusing optics: MLLs, FZPs, Kinoforms, and KBs. To date, the microscopes with the highest positioning/scanning performance are designed for FZPs. MLLs and KBs require a larger number of degrees of freedom for alignment. The requirement for short-format Kinoforms is similar to FZP. These optics also have different requirements for a beam stop and order-sorting aperture, and working distance from the optics to the sample. The HXN microscope requires different interchangeable optic modules to accommodate these different requirements.
- Sample environment: Materials science applications require the ability to control the temperature and atmosphere. Soft materials require cryostats to reduce the level of radiation damage. The ability to maintain and control temperatures from ~ –150˚C to ~300˚C is required.

Meeting all of the above requirements is extremely challenging. The final set of requirements will be determined through interaction with potential vendors and the scientific priorities set by the HXN BAT.

3.2 HXN Detectors

The HXN experiments require multiple detectors: an XRF detector for elemental mapping, a 2D area detector for coherent diffraction imaging and differential phase contrast, a 2D area detector for nanodiffraction, and a high-resolution (lens-coupled, ~1μm resolution) CCD detector. A multi-element silicon drift diode (SDD) detector (i.e. multi-element Vortex) is commercially avaialbe. As a commercial option, a direct detection CCD can be used for coherent diffraction imaging and nanodiffraction.

The experiments at the HXN beamline can be significantly benefited by advanced x-ray detectors that are currently being developed. Dr. Peter Siddons and his team at BNL have developed the MAIA detector for high-throughput fluorescence measurement. This detector could be a candidate for the XRF detector of the HXN. Integrating this detector with the HXN microscope requires engineering efforts, working with a potential vendor for the HXN microscope. In order to implement ptychography-based coherent diffraction imaging with fluorescence mapping, a fast forward-direction detector must be used. This detector should have a minimum of 256x256 elements with ~200 μm pixel size with the same timing response as the MAIA detector, in order for them to be used together. Development of such a detector requires close collaboration with Dr. Siddons' group. Nanodiffraction experiments can be best benefited by a pixel array detector with ~1k x 1k pixels with a pixel size of ~150 μm or smaller with a large dynamic range ($>10^4$) and a fast readout time (<10 ms) rather than a CCD detector.

4 SPECIAL BEAMLINE REQUIREMENTS

4.1 Satellite Building and Endstation

The most important requirement of the HXN beamline is the remote satellite building to house the HXN endstation, designed and constructed to meet vibration and temperature stability adequate for maintaining a 1nm-sized x-ray beam over a period longer than 12 hours. Since such a facility has not been constructed before, the specifications of the endstation floor vibration, temperature stability, and acceptable acoustic noise level can only be inferred from the requirements of state-of- the-art electron microscopy facilities.

To help define the specifications and requirements for the HXN satellite building and the endstation, a workshop was held on June 29, 2009 with scientists, engineers, and architects from HDR (the architectural firm, contracted to build the NSLS-II LOB). The following primary requirements and specifications are currently under discussion.

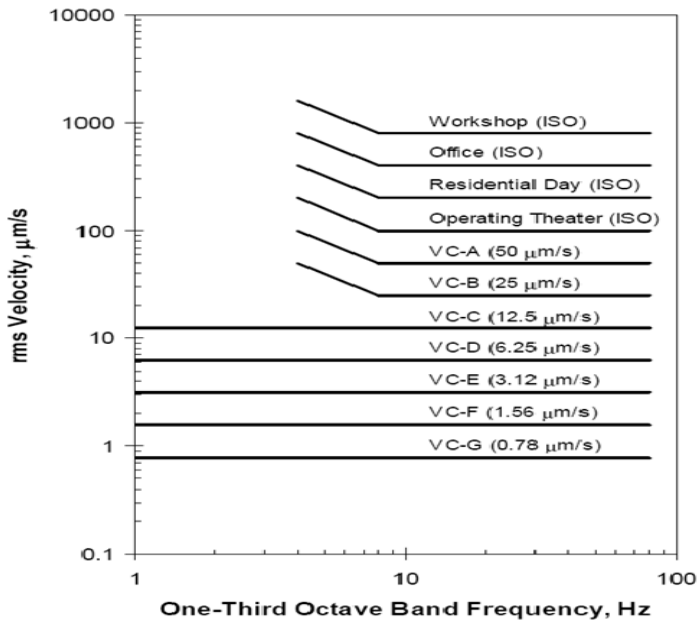

Figure 4.1: Various vibration specifications. Vibration criterion, VC-F, will be used as a vibration requirement for the HXN end-station floor.

1. The HXN satellite building must be physically isolated from the NSLS-II storage ring building and the nearby LOB.
2. The utilities (electricity, ventilation, water, and nitrogen gas) will be fed from the nearby LOB with careful consideration for vibration damping.
3. The external shell, wall, and roof structure are supported by an isolated footing structure, separated by the floor structure under the HXN endstation. The external shell and wall must have sufficient insulation to prevent temperature fluctuation of the interior due to temperature change from day to night and season to season.
4. The endstation must be constructed with a concrete wall of 8-inch thickness. The interior dimension of the endstation is 20 m long, 5 m wide, and 3.5 m high.
5. The electronic or mechanical equipment, generating acoustic vibration and heat, will be isolated from the user area and also the endstation on a separate floor structure.
6. To maximize the structural filtering of low frequency ground vibration, the user area and the endstation will share the same concrete floor. The concrete floor under the endstation will be 1 m thick. To prevent vibrations from the user area from reaching the HXN microscope, the user area will be covered with "CONCREDAMP," a concrete additive that damps vibration and noise. In addition, a small, narrow trench will be made around the outer wall of the endstation, to prevent surface vibration waves from traveling into the endstation.
7. The noise level within the endstation will be maintained at 40dBA or lower. The outer and interior wall of the endstation must be covered with acoustic damping materials. The water flow through the utility line will be regulated to meet the noise requirement.
8. Noisy or heat generating instruments will be enclosed within a water-cooled instrument rack.
9. The temperature in the user area will be maintained at 24°C ±1.0°C, at all times. The maximum temperature fluctuation over 1 hr period will be ±0.5°C. The temperature in the endstation will be 24±0.05°C. The maximum

temperature fluctuation over a 1-hr period will be ±0.02°C. A local area around the HXN microscope will be enclosed, in order to maintain higher degree of temperature stability.

10. An airlock door will be installed in order to minimize the air exchange in and out of the endstation from the user area.

More complete specifications for the satellite building can be found in Experimental Facilities **R**equirements, **S**pecifications and **I**nterfaces (RSI) document for the Hard X-ray Nanoprobe Beamline Satellite Building.

4.2 Data Transfer Rates

The HXN beamline will employ multiple detectors during the experiment. Up to 10 or more detectors can be used at the same time. The table below summarizes the estimated data production rate at the HXN beamline.

Table 4.1. Estimated Data Production Rate at the HXN Beamline.

Detector	Data production	Data rate
Multiple element energy dispersive detector	96 element operating at 100 Hz or higher	20 MB/sec
1k x 1k pixel array detector	4 MB at 100Hz	400 MB/sec
4k x 4k CCD detector	96 MB at 0.2Hz	19.2 MB/sec
Ion chambers and other 1D detectors	Insignificant	
beam position monitors	Insignificant	

APPENDIX 1: SCHEDULE

Construction of HXN Beamline

September	2009	Complete conceptual design report
September	2010	Complete preliminary design report
November	2010	Technical design – approval of long lead term procurement
January	2011	Start long lead time procurements (monochromator, mirrors, enclosures,…)
April	2011	Complete final design of beamline major components
February	2012	Complete final design report Approval of start of beamline construction - beneficial occupancy of experimental floor
February	2012	Start installation
April	2012	Start other procurements
May	2012	Start sub-system testing
November	2012	Complete long lead time procurements
August	2013	End procurement
August	2013	Start integrated testing
January	2014	Complete installation
February	2014	Complete sub-system testing
May	2014	Complete integrated testing – beamline available for commissioning
June	2015	**CD-4**, approve start of operations

Planned Tasks and Milestones for 1nm Spatial Resolution R&D

Since the conceptual design, construction, and operation of the HXN beamline are intimately connected by the outcome of the supporting R&D program, the conceptual design report summarizes planned key tasks and milestones. The dates associated with the specific tasks and milestone could change due to the unforseen technical challenges.

- MLL deposition system fully commissioned: FY10 Q4
- First wedged MLL: middle of FY11 Q2
- First 100 μm-aperture MLL with through-center growth: FY12 Q3
- First 1nm MLL deposited: FY13 Q4
- First 1nm wedged MLL with 100 μm aperture: FY14 Q2
- MLL optimized for 8-10 keV: FY15 Q2
- Develop phase-retrieval methods for accurate determination of focused beam size (< 10 nm): FY10 Q4
- Develop a robust method to assemble two MLLs into a single optic: FY11 Q2~FY14 Q4

Planned Tasks and Milestones for Nanopositioning R&D

- Establish a formal joint work project with the APS for development of the HXN prototype instrument: started in Sept, 2009.
- Commence building up Nanopositioning Lab in BNL/building 703 in order to evaluate laser interferometers and nanopositioning devices: FY10 Q3
- Evaluate vibration damping options: FY11 Q4
- Reach a critical decision on the components of the HXN prototype: FY11 Q4
- Detailed design fo the HXN prototype instrument: FY12 Q1
- Construction of the HXN prototype instrument (initial configuration for further refinement): FY12 Q4
- Reach a critical procurement decision on the HXN microscope, including detailed specifications and capabilities, for construction by a vendor: FY12 Q1
- Installation and testing of the HXN microscope: FY14 Q3
- Commissioning of the HXN microscope: FY14 Q3~FY15Q3
- User experiments using the HXN microscope: FY15 Q2
- Continue 1nm R&D at the HXN beamline using the HXN prototype after the commissioning of the HXN beamline.

APPENDIX 2: CONSIDERATIONS FOR HXN BEAMLINE SITE

Memorandum

Date: March 12, 2010
To: S. Dierker, M. Fallier, Q. Shen
From: Nick Simos
Subject: NSLS-II Nanoprobe Beamline Location Optimization – Site Vibration Aspects

This memo/technical note summarizes the results of the studies conducted to quantify the ground vibration at the two potential locations of the nanoprobe endstation (attached to LOB-2 or to LOB-3) and makes recommendations as to which of the two locations is more favorable and why.

The evaluation of the position of the nanoprobe station was based on:

1. NSLS-II site ground vibration spatial variability (affected by operating systems over the BNL site such as NSLS, CFN, etc., traffic on site, and the effect of the Long Island Expressway)
2. The effect of heavy traffic on Brookhaven Avenue (what happens at the limit of moving loads such as a 20-ton truck traveling at 30 mph?).
3. The effect of NSLS-II service building operations and the contribution toward noise reaching the nanoprobe station

The assessment of these different sources, whose combined effect should provide a clear picture as to which location for the nanoprobe end station is most appropriate, is supported by extensive field tests and accompanied by large-scale mathematical models. In particular, to address the effect of "extreme" traffic in the vicinity of NSLS-II a dedicated field test was performed that utilized a 20-ton, 3-axle large truck traveling along Brookhaven Avenue at different speeds (30 mph and 15 mph). A specially designed model describing the large truck pass as a moving source with a complicated dynamic signature was introduced as the stimuli in the dynamic model. Successful matching of such moving loads has been demonstrated in the past by the author, where simulated data/predictions compared very well with actual data.

Results associated with the three major sources indicated above are listed in three separate sections, namely M.1, M.2 and M.3. The findings are summarized as follows:

Regarding the spatial variability of the background vibration over the NSLS-II site, LOB-3 position is more favorable. In particular it was found that the "local" noise consisting of operations on site (CFN, NSLS, etc.) and BNL traffic during the day has a significant contribution which more pronounced at the LOB-2 location. The LI Expressway effect is similar for both locations.

Regarding the "occasional" extreme effect of large trucks traveling on-site and near NSLS-II, it is demonstrated through field tests and the subsequent analytical effort that location LOB-3 will be immune to such traffic while the LOB-2 location will exceed its stability requirements for the period the load will be in the vicinity of NSLS-II. In particular, ground displacements in the excess of 300 nm will be felt at the LOB-2 location for a short period, while this value will be ~15 nm at LOB-3, indicating that it will barely be felt since it will blend with the background.

Regarding the NSLS-II service building operations, the effect will be both small and similar for both choices (LOB-2 or LOB-3), given the similarity in the layout and their relative position to the SB structures.

The bottom line, based on this extensive evaluation, is that the LOB-3 position of the nanoprobe station is a more favorable position than its LOB-2 counterpart, and it is recommended as the optimal location for the vibration-sensitive endstation.

Nicholas Simos, PhD, PE
NSLS II Project

M.1: NSLS-II Site Spatial Variability of Ground Vibration

To assess the differences that may exist at the two potential locations in terms of the background ground vibration, a series of measurements were performed on the footprint of the NSLS-II and in the surrounding space, especially in terms of the NSLS-II position with the Long Island Expressway (LIE). It is expected that over the NSLS-II footprint, and thus the nanoprobe locations, will exist spatial variability of the ground vibration. In other words the vibration field will not be uniform. The deviation is expected to vary depending on the time of day and the day of the week (i.e., weekday vs. weekend). This variability, which will have an impact on the nanoprobe endstation location, is primarily the result of noise sources within BNL (CFN, NSLS, and other nearby operations), traffic-borne vibration from within BNL, and the traffic-borne ground vibrations reaching the site from the LIE.

To quantify the effects, measurements were performed both at the NSLS-II site and on the space separating LIE from NSLS-II, aiming to establish attenuation characteristics. Figure M.2-1 shows the approximate locations where measurements were performed. S1 is approximately 200 ft from the LIE, S2 ~1000 ft, S3 ~2000 ft', and S4, ~2200 ft. Site station #5 was approximately situated where the nanoprobe station will be if it is to be placed by LOB-2. Refer to figures M.1-2, 3, and 4.

The important findings are the following. The LIE effect attenuates as one approaches the NSLS-II site. There it is the locally-borne traffic and other sources that affect the background noise at the site. This is clearly demonstrated by the spectra of Figures M.1-2 and M.1-3, where the cultural noise in mid-day increases on the site. Measurements at 5 a.m. on Sunday clearly eliminate the local effect. Given that the LOB-3 option moves the nanoprobe station further from the local sources, then it is safe to assess that the effect of the local sources will be less on LOB-3 option than the LOB-2 counterpart.

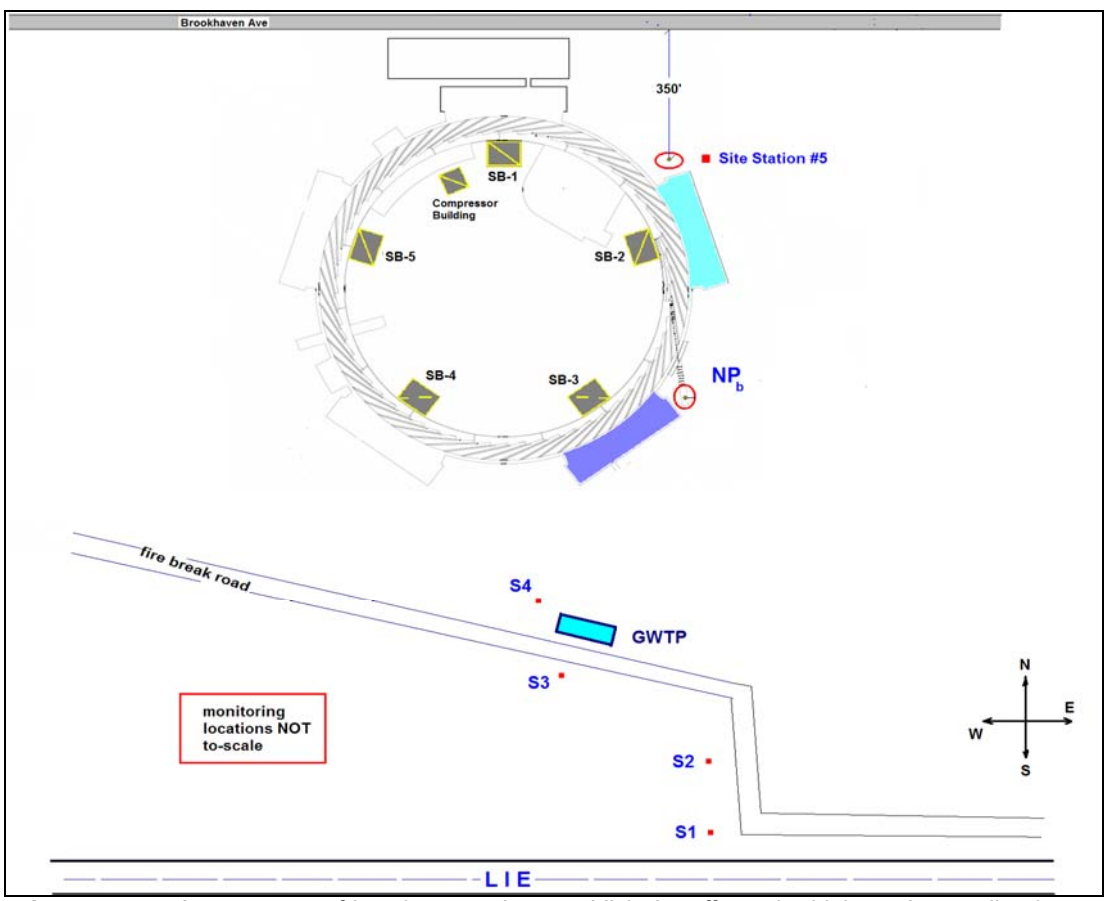

Figure M.1-1: Arrangement of locations used to establish the effects the highway borne-vibration at NSLS2 and the BNL site source contribution to NSLS2 site background noise

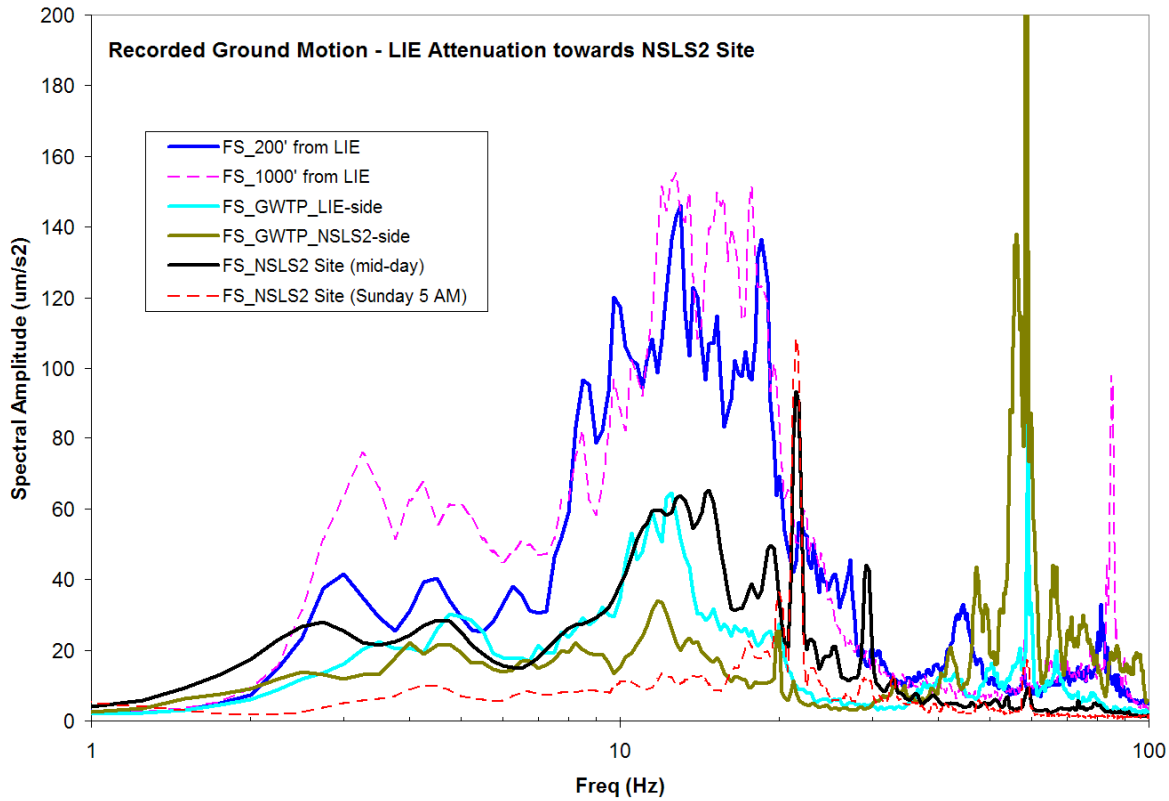

Figure M.1-2. Ground motion spectra over the different monitoring locations indicating the traffic-borne vibration (<12 Hz), as well as operating system signatures that exist in the proximity of the NSLS2 site.

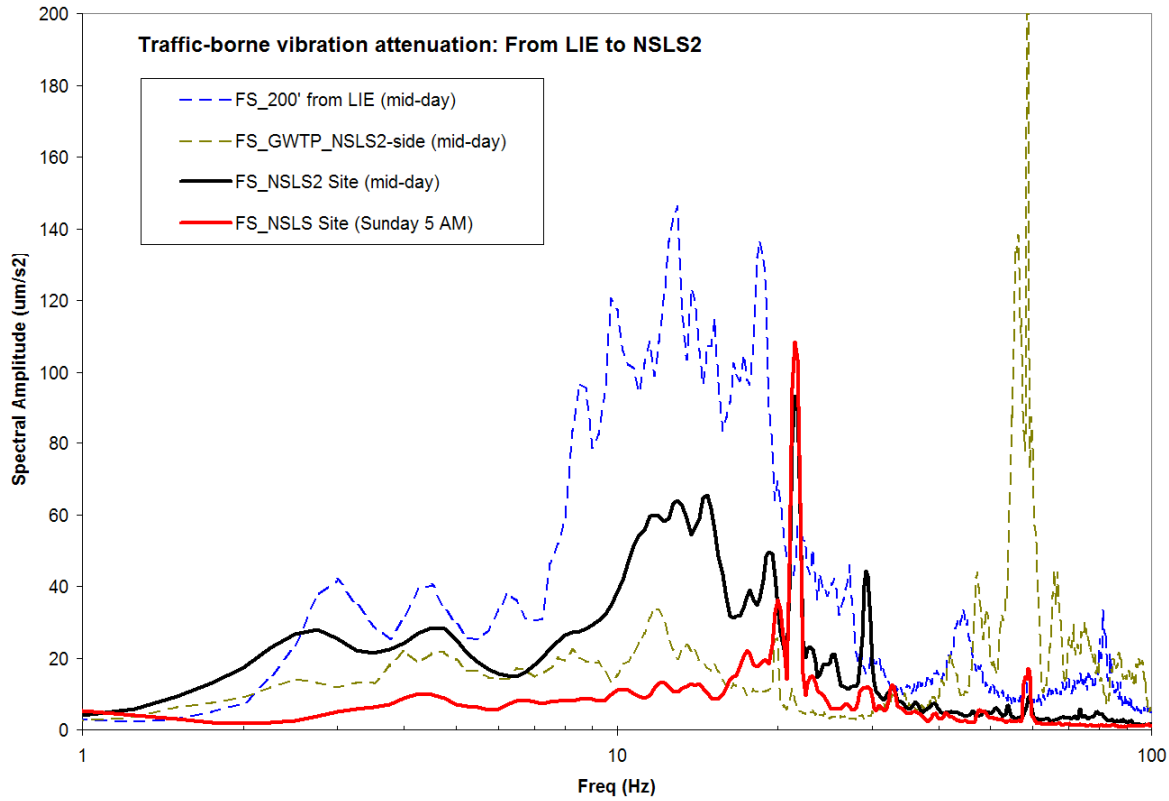

Figure M.1-3. Ground motion spectra depicting the effect of LIE and the local sources at NSLS2 site.

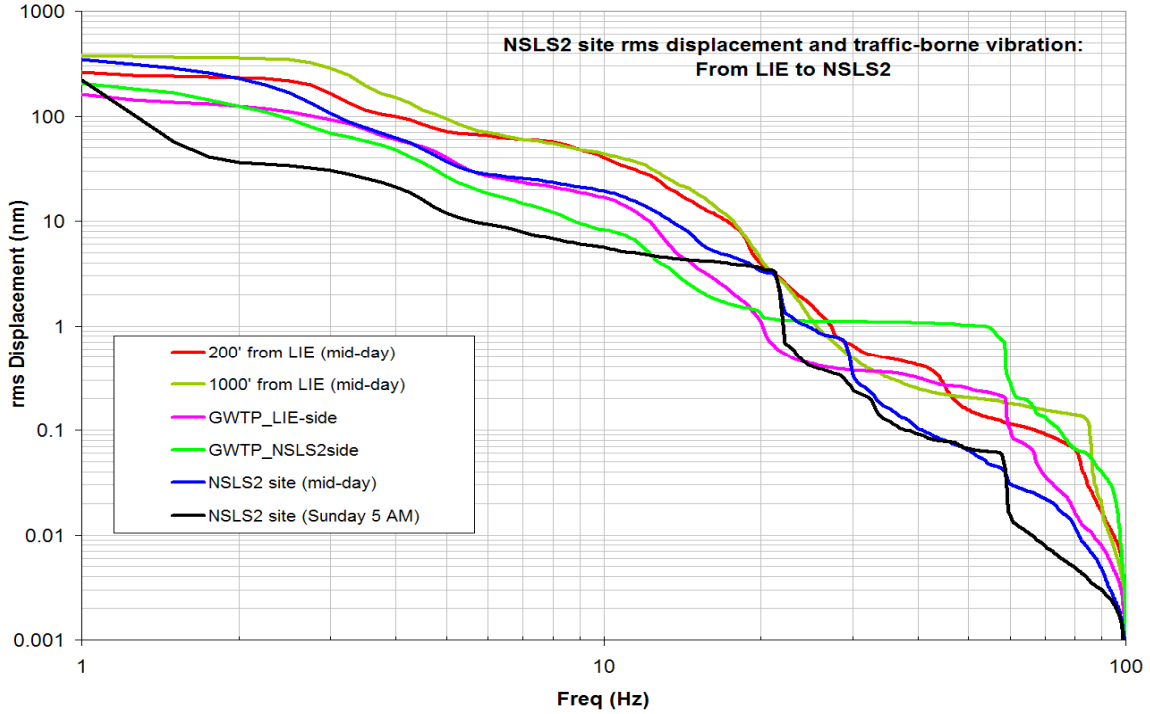

Figure M.1-4. Ground displacements (rms) at different locations relative to LIE and different times.

M.2 Field Test for "Extreme" Traffic on Brookhaven Ave. and Influence on Nanoprobe

To quantify the effect of an occasional extreme transient noise, such as a heavy truck traveling on the roads near the NSLS-II and in particular on Brookhaven Avenue, a field test was conducted. The aim was to assess the attenuation characteristics (or distance effects) of the induced ground vibration and to quantify the vibration levels that will be felt at different locations and in particular the two positions of the nanoprobe station being considered.

A 20-ton, 3-axle truck was used for the field test. The truck travelled several times on Brookhaven Avenue, as shown in Figure M.2-1, with velocities of 30 and 15 mph, and ground vibration records were captured at locations P1, P2, and P2. These ground accelerations were analyzed and the results were used in the assessment. Important to point out is that the monitoring location P3 is at approximately the same distance from Brookhaven Ave, as is the LOB-2 option for the nanoprobe (P3 is at 400 ft while LOB-2 option at ~350 ft). The LOB-3 option is ~990 ft from Brookhaven Avenue. No direct measurements were made at the LOB-3 location, since no monitoring stations existed at the vicinity. The field test records and the benchmarked numerical model were eventually used to extrapolate the effects on the LOB-3 location.

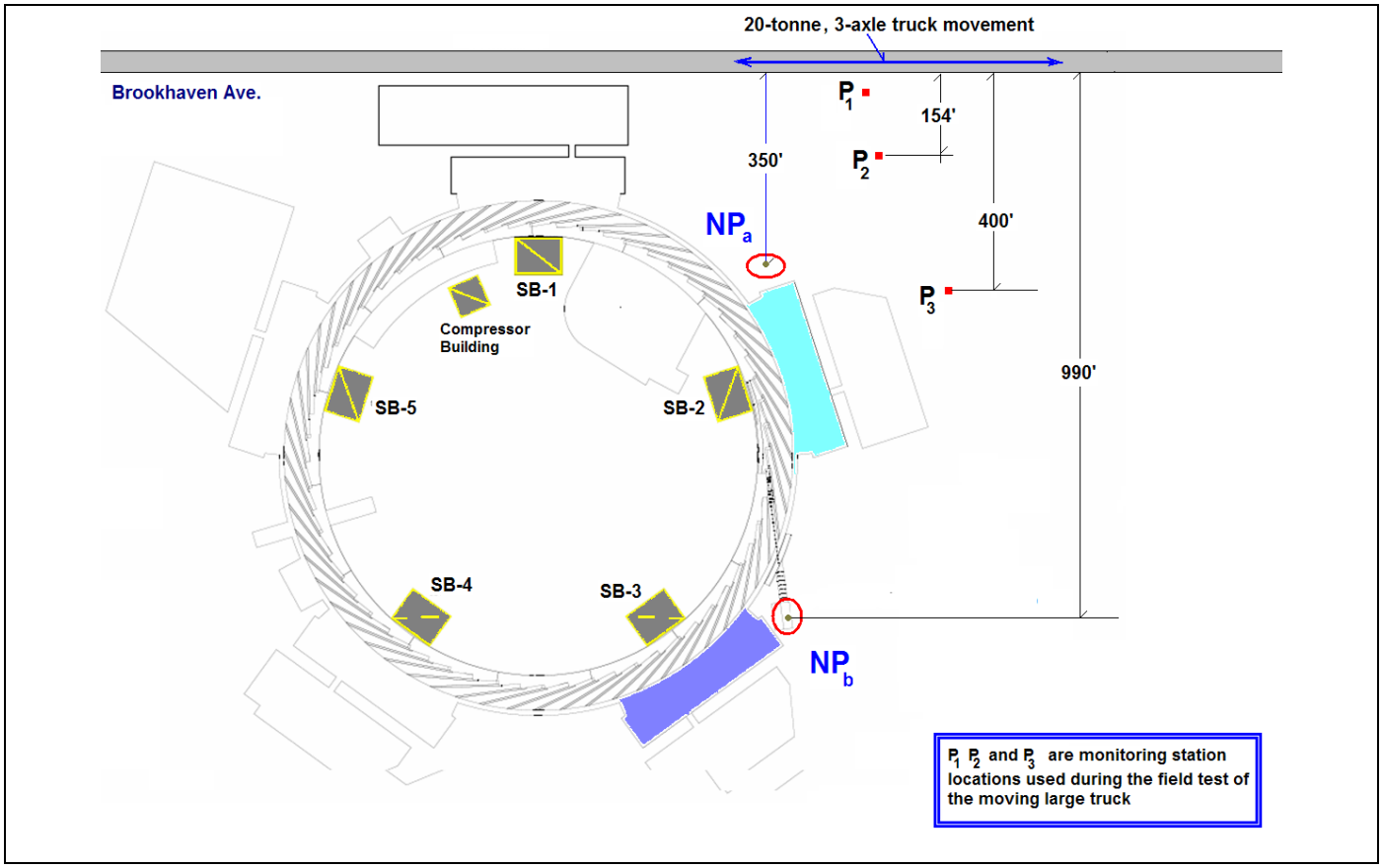

Figure M.2-1. Layout of the field test using a 20-ton moving truck and assessing the ground vibration at the NSLS-II.

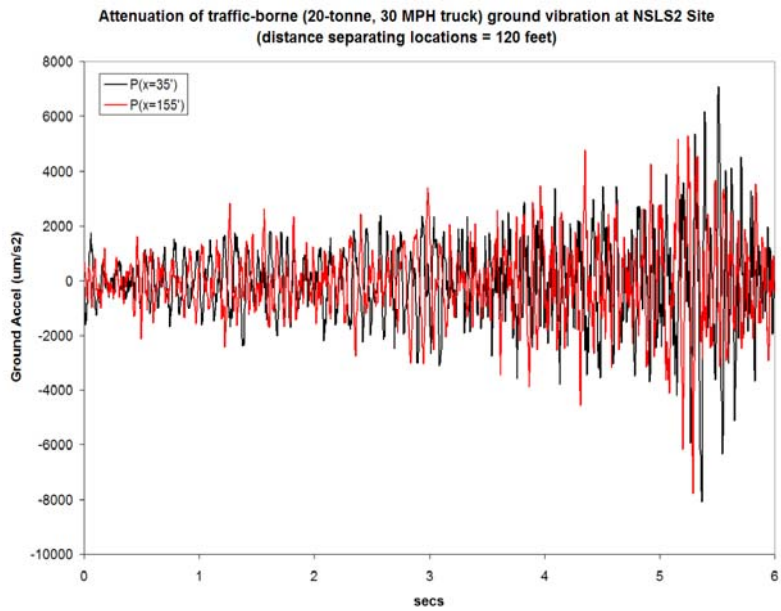

Figure M.2-2. Recorded ground motion depicting attenuation with distance of 120 ft (monitoring stations P1 and P2).

site.

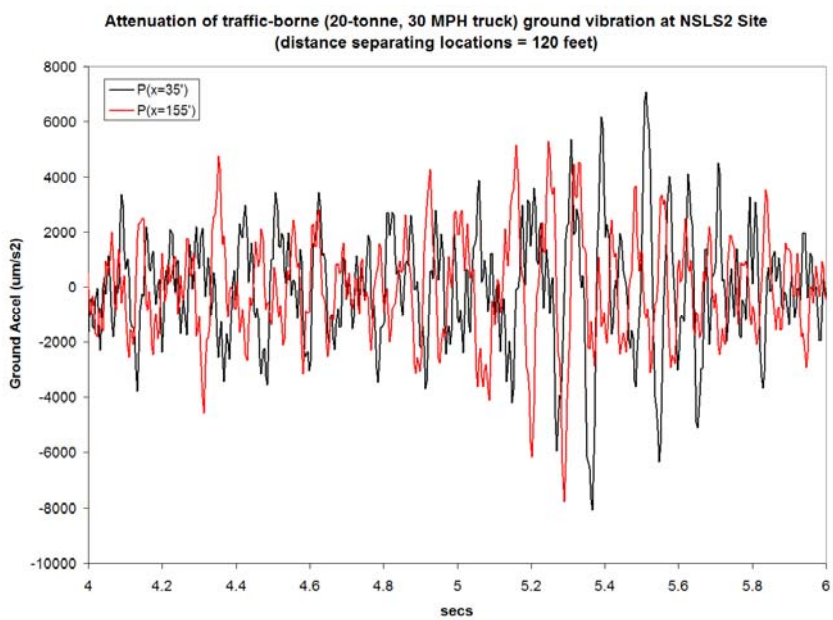

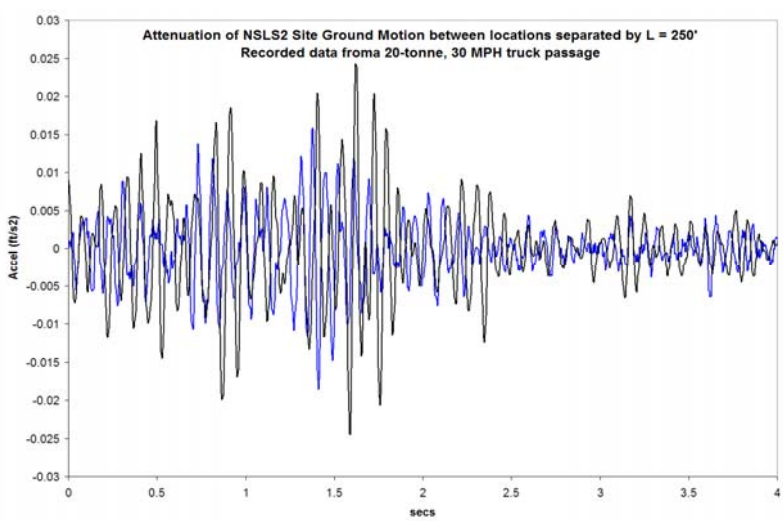

Figure M.2-3: Recorded ground motion and attenuation with distance of 250 ft (monitoring stations P2 and P3).

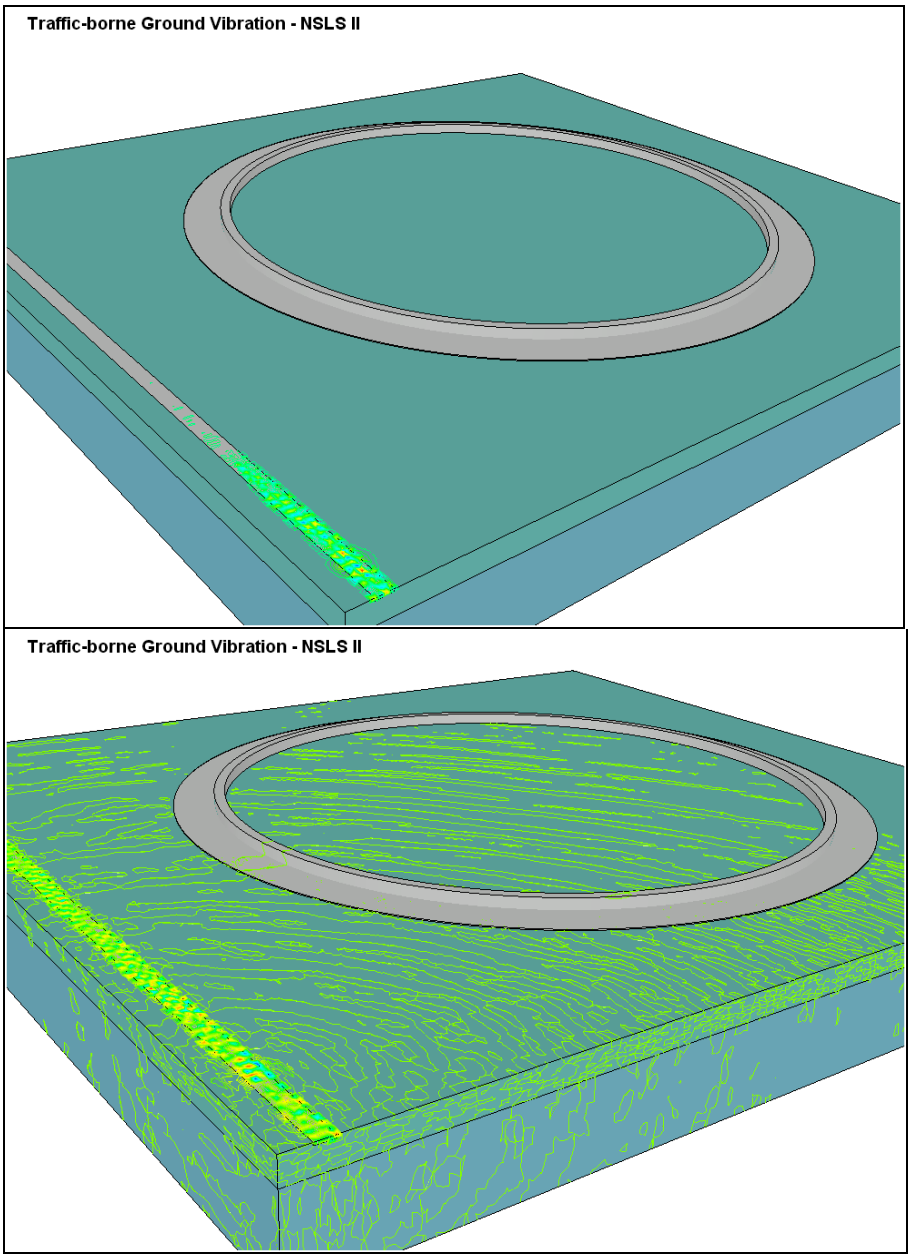

Figure M.2-4: Mathematical model used to simulate the 20-ton, 3-axle truck mph.

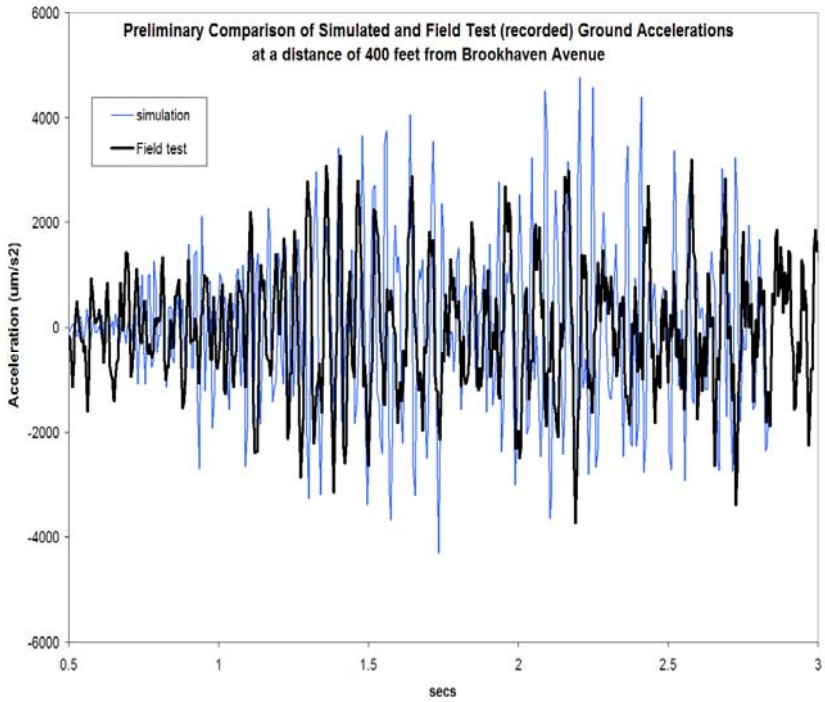

Figure M.2-5. Preliminary comparison of the ground vibration transient between the field test and the prediction through the simulation model at a distance of 400 ft from Brookhaven Avenue.

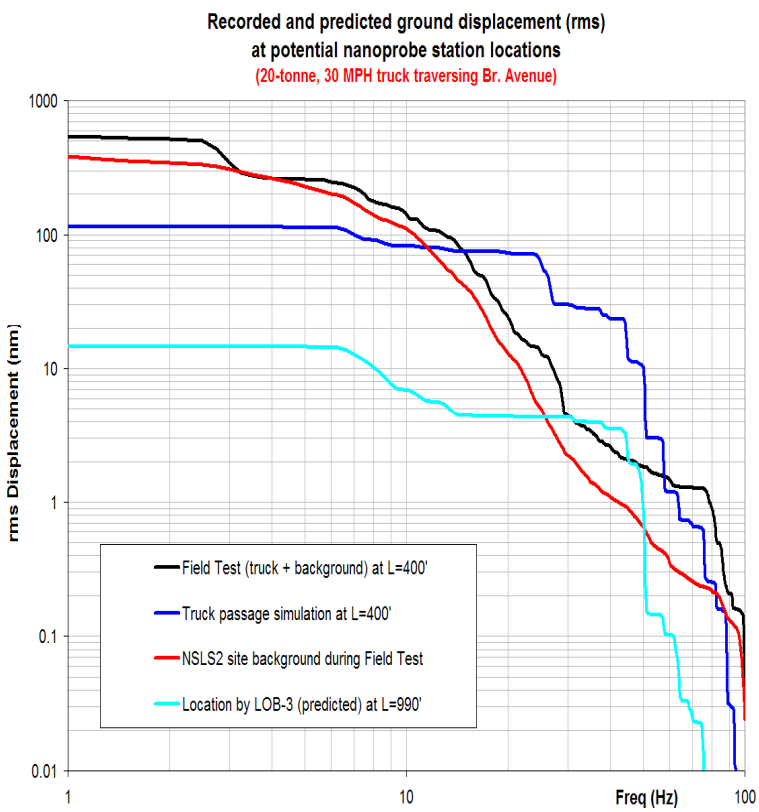

Figure M.2-6. Ground displacement (rms) based on actual test data and numerical predictions. Of importance is the extrapolation, based on the numerical model and the attenuation characteristics recorded during the field test, of the data to the LOB-3 location. Based on these findings, the effect of the large truck at that distance will be blended with the background (it shows ~14 nm for frequencies > 2 Hz). This is not the case with LOB-2 where the passage of the truck will be felt.

APPENDIX 3 LIST OF BEAMLINE COMPONENTS

Item	Description	Part Number	Symbol	Z(m)	Location
	Fixed Mask	(SR-FE-IDN1-1100)	FM		Front End
	White Beam Slits	(SR-FE-IDN1-1100)	S1	16.4	Front End
	Storage Ring Wall				
1	Gate Valve	XF-BL-HXN-GateValve	GV1	25.6	FOE
2	Aperture Plate	XF-BL-HXN-AperturePlate	AP	25.7	FOE
3	Diagnostic Chamber	XF-BL-HXN-DiagnosticChamber	DC1	25.9	FOE
4	White Beam Filters	XF-BL-HXN-WhiteBeamFilters	WBF	26.3	FOE
5	Be Window	XF-BL-HXN-Be-Window	BW1	26.6	FOE
6	Horizontal Collimating Mirror	XF-BL-HXN-Horizontal-Collimating-Mirror	M1	27.5	FOE
7	Gate Valve	XF-BL-HXN-GateValve	GV2	28.4	FOE
8	Bremsstrahlung Collimator	XF-BL-HXN-BremsstrahlungCollimator	CO	28.6	FOE
9	Pink Beam Slits	XF-BL-HXN-PinkBeamSlits	S2	29.0	FOE
10	Pink Beam Screen Monitor	XF-BL-HXN-PinkBeamScreenMonitor	PBSM	29.2	FOE
11	Gate Valve	XF-BL-HXN-GateValve	GV3	29.5	FOE
12	Monochromator, Horizontal Double Crystal	XF-CM-1028	DCM1	30.2	FOE
13	White beam Stop	XF-BL-HXN-WhiteBeamStop	BS	30.7	FOE
14	Diagnostic Chamber	XF-BL-HXN-DiagnosticChamber	DC2	30.9	FOE
15	Gate Valve	XF-BL-HXN-GateValve	GV4	31.3	FOE
16	Horizontal Focusing Mirror	XF-BL-HXN-HorizontalFocusingMirror	M2	32.1	FOE
17	Gate Valve	XF-BL-HXN-GateValve	GV5	33.0	FOE
18	Mono Beam Position Monitor	XF-BL-HXN-MonoBeamPositionMonitor	BPM1	33.3	FOE
19	Vertical Focusing Mirror	XF-BL-HXN-VerticalFocusingMirror	M3	34.1	FOE
20	Vertical Flat Mirror	XF-BL-HXN-VerticalFlatMirror	M4	35.4	FOE
21	Gate Valve	XF-BL-HXN-GateValve	GV6	36.0	FOE
22	Bremsstrahlung Stop	XF-BL-HXN-BremsstrahlungStop	BS	36.3	FOE
23	Mono Beam Position Monitor	XF-BL-HXN-MonoBeamPositionMonitor	BPM2	36.8	FOE
	Long BeamPipe				FOE
24	Mono Beam Shutter	XF-BL-HXN-MonoShutter	MS1	39.5	FOE
25	Gate Valve	XF-BL-HXN-GateValve	GV7	39.9	FOE
	Hutch 1 Downstream Wall			40.0	FOE
	Hutch 2 Upstream Wall			57.5	Mono Hutch
26	Gate Valve	XF-BL-HXN-GateValve	GV8	57.9	Mono Hutch
27	Be Window	XF-BL-HXN-BeWindow	BW2	58.0	Mono Hutch
	Long Beampipe				Mono Hutch
28	Be Window	XF-BL-HXN-BeWindow	BW3	61.0	Mono Hutch
29	Mono Beam Position Monitor	XF-BL-HXN-MonoBeamPositionMonitor	BPM3	61.3	Mono Hutch
30	Gate Valve	XF-BL-HXN-GateValve	GV9	61.7	Mono Hutch
31	Secondary Source Aperture	XF-BL-HXN-SecondSourceAperture	SSA1	62.0	Mono Hutch
32	Gate Valve	XF-BL-HXN-GateValve	GV10	63.8	Mono Hutch
33	Mono Beam Shutter	XF-BL-HXN-MonoShutter	MS2	64.2	Mono Hutch
	Hutch 2 Downstream Wall			64.5	Mono Hutch
	Hutch 3 Upstream Wall			92.9	Endstation
34	Gate Valve	XF-BL-HXN-GateValve	GV11	93.1	Endstation
35	Mono Beam Position Monitor	XF-BL-HXN-MonoBeamPositionMonitor	BPM4	93.4	Endstation
36	Secondary Source Aperture	XF-BL-HXN-SecondSourceAperture	SSA2	94.0	Endstation
37	High-Resolution Monochromator (mature phase)	XF-BL-HXN-HighResolution Monochrom.	DCM2	95.0	Endstation
38	Be Window	XF-BL-HXN-BeWindow	BW4	95.5	Endstation
	Long Beampipe				Endstation
39	HXN Microscope	XF-BL-HXN-Microscope	MIC	108.0	Endstation
	Hutch 3 Downstream Wall			113.0	Endstation

APPENDIX 4 REFERENCE DRAWINGS

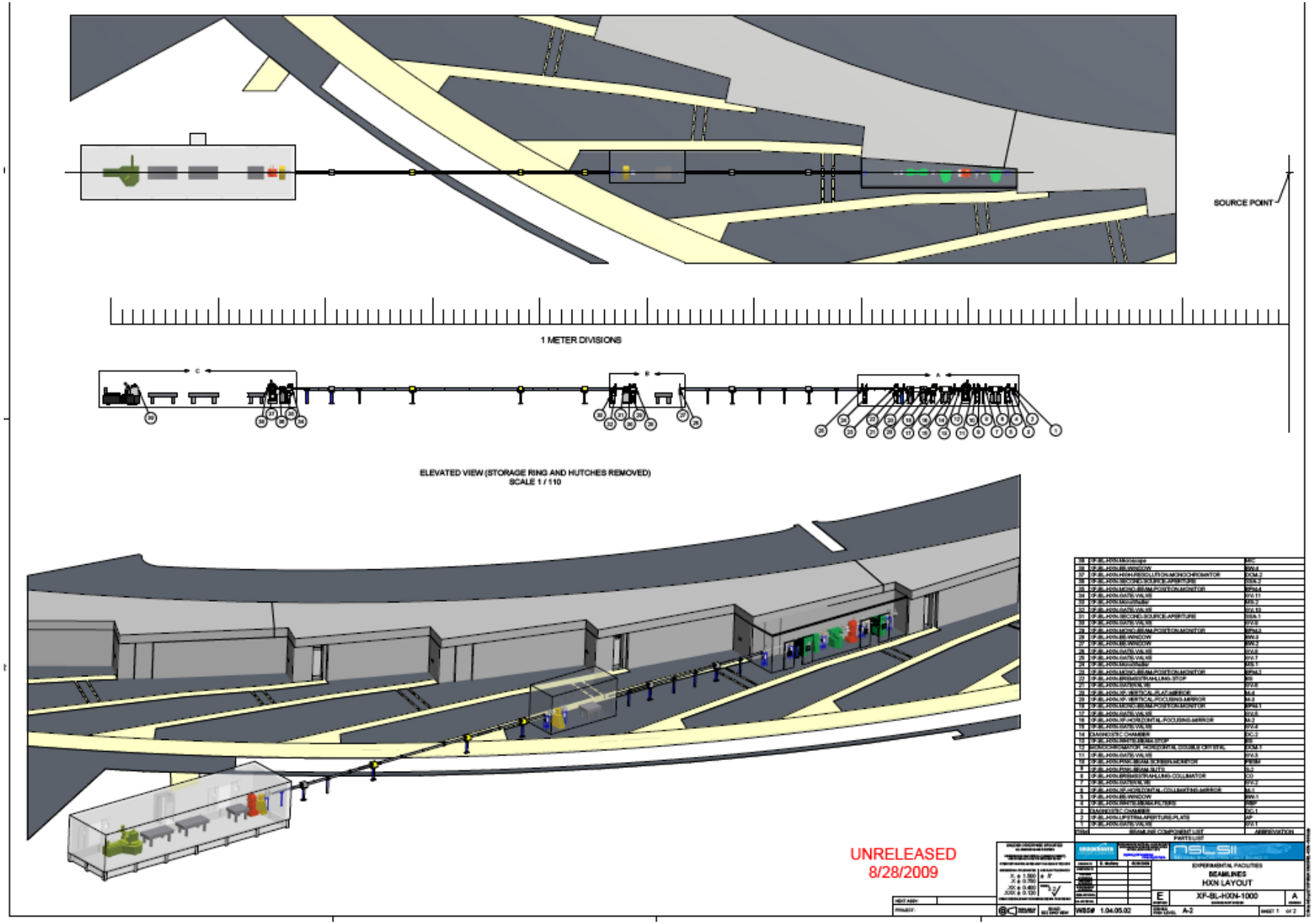
SOURCE POINT
1 METER DIVISIONS
ELEVATED VIEW (STORAGE RING AND HUTCHES REMOVED)
SCALE 1 / 110
UNRELEASED
8/28/2009
BEAMLINES
HXN LAYOUT
XF-BL-HXN-1000
A-2

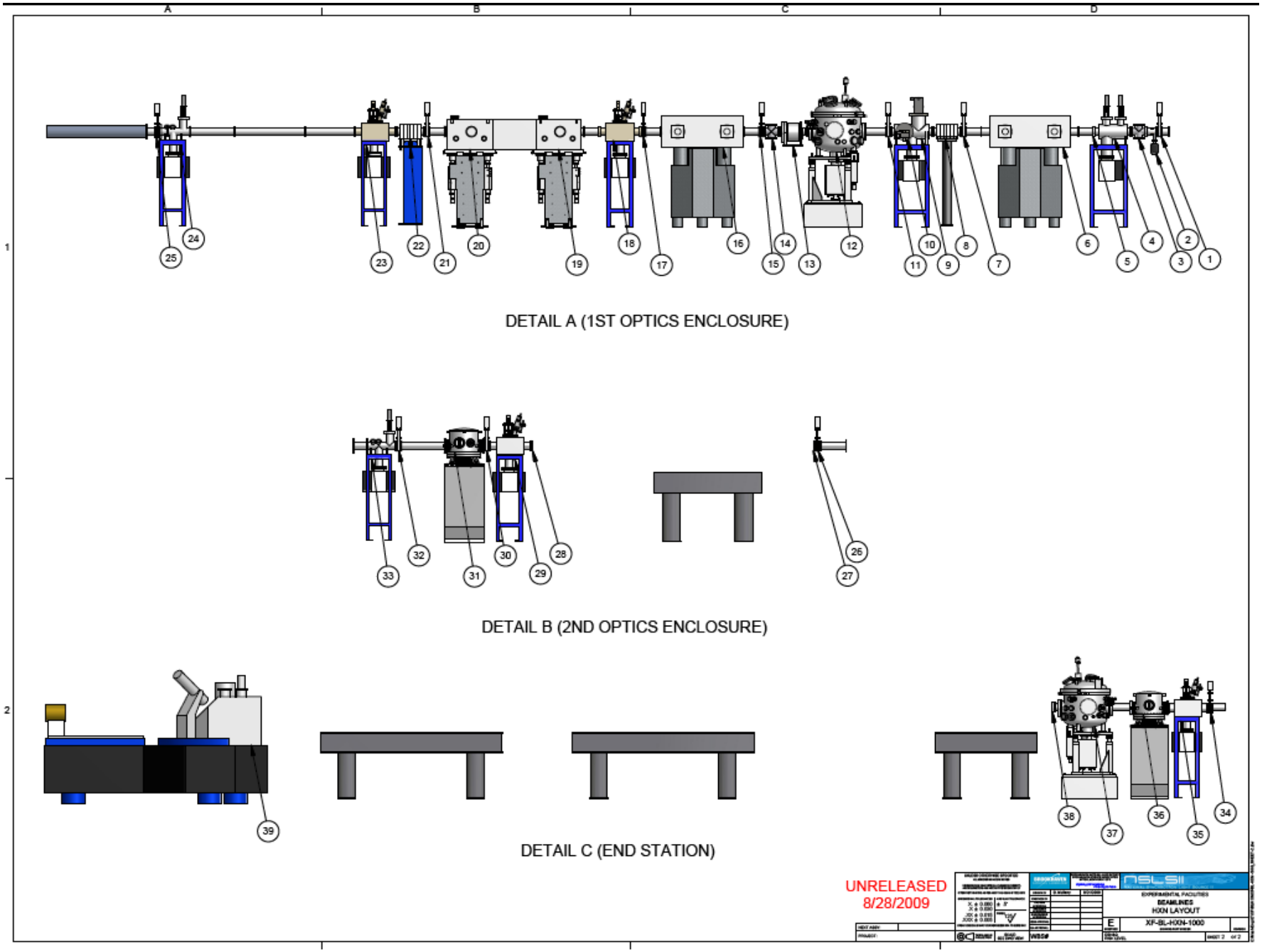
DETAIL A (1ST OPTICS ENCLOSURE)
DETAIL B (2ND OPTICS ENCLOSURE)
DETAIL C (END STATION)
UNRELEASED
8/28/2009
BEAMLINES
HXN LAYOUT
XF-BL-HXN-1000

Intentionally blank.